AGU PUBLICATIONS

JGR

Journal of Geophysical Research: Earth Surface

RESEARCH ARTICLE
10.1002/2015JF003580

Key Points:
- Glacial simulations can be nudged to ICE-6G_C over relevant timescales
- GIA-based reconstruction is shown consistent with ice sheet dynamics
- Nudging brackets poorly constrained BCs and parameterizations

Correspondence to:
G. R. Stuhne,
gordan@atmosp.physics.utoronto.ca

Citation:
Stuhne, G. R., and W. R. Peltier (2015), Reconciling the ICE-6G_C reconstruction of glacial chronology with ice sheet dynamics: The cases of Greenland and Antarctica, *J. Geophys. Res. Earth Surf.*, *120*, 1841–1865, doi:10.1002/2015JF003580.

Received 9 APR 2015
Accepted 19 AUG 2015
Accepted article online 24 AUG 2015
Published online 20 SEP 2015

Reconciling the ICE-6G_C reconstruction of glacial chronology with ice sheet dynamics: The cases of Greenland and Antarctica

G. R. Stuhne[1] and W. R. Peltier[1]

[1]Department of Physics, University of Toronto, Toronto, Ontario, Canada

Abstract We describe a theoretical and numerical framework that has been developed to investigate the compatibility of the ICE-6G_C reconstruction of the glaciation histories of the Greenland and Antarctic ice sheets with the latest understanding of ice physics. The ICE-6G_C reconstruction has been produced solely on the basis of the theory of the glacial isostatic adjustment (GIA) process, and it has remained an issue as to whether such reconstructions of the time-dependent thickness variations of grounded continental ice sheets were compatible with physics-based ice mechanical considerations. Our analyses focus on the evolution over the last glacial cycle of these extent ice sheet complexes and demonstrate that the GIA-inferred models are entirely consistent with such considerations when uncertainties in (net) mass balance history are taken fully into account.

1. Introduction

Over the past several decades increasingly detailed models of the evolution of continental ice cover through the most recent 100,000 year glacial cycle of the Late Quaternary Period have been produced through application of the theory of the glacial isostatic adjustment (GIA) process [*Peltier*, 1974, 1976a, 1976b; *Peltier and Andrews*, 1976; *Farrell and Clark*, 1976; *Clark et al.*, 1978; *Peltier et al.*, 1978] as recently reviewed in detail in *Peltier* [1998, 2007], and *Peltier et al.* [2015]. This theoretical structure, which is now being widely employed internationally, considers leading order mass-balance variations independently of detailed assumptions concerning either past climate variations or ice sheet dynamical evolution. It has been qualitatively understood since the nineteenth century that the growth and decay of ancient continental ice sheets have left their signatures in modern physical geography through coupling to the deformations of the solid Earth and associated sea level change, and the GIA methodology formulates these ideas in a quantitative, gravitationally self-consistent theory embodied in an integral Sea Level Equation (SLE). Given an assumed history of land ice thickness variations and a model of the radial viscoelastic structure of the planet, the SLE predicts the variations of the level of the sea with respect to the continuously deforming surface of the solid Earth that should be observed along any coastline from which appropriately dated histories of relative sea level (RSL) are available. Given a global database of RSL histories and measurements of associated observables, the combination of observations and theory poses an inverse problem for the history of land ice thickness variations and the radial viscoelastic structure, the solution of which reconciles the observations with a consistent history of land ice thickness variations. Even though the theoretical structure is highly nonlinear and this inverse problem therefore a formidable one to solve in principle, there exists a wealth of information available whereby highly accurate first approximations to the required global glaciation history may be constructed. This methodology has led to a series of successively refined histories beginning with the ICE-1 history of *Peltier and Andrews* [1976], the ICE-3G history of *Tushingham and Peltier* [1991], the ICE-4G history of *Peltier* [1996], the ICE-5G history of *Peltier* [2004], and, most recently, the ICE-6G_C history of *Argus et al.* [2014] and *Peltier et al.* [2015] which will be the focus of the present paper. ICE-6G_C and the accompanying VM5a reconstruction of the radial viscoelastic structure evolved from earlier versions by fitting SLE predictions to an extensive and expanding database of observations consisting of RSL histories, GPS and other space geodetic measurements of the present-day vertical and horizontal motion of the crust, and exposure age dating of ice thickness variations (in Antarctica).

While fundamentally based only upon the constraints provided by the GIA process, the ICE-6G_C (VM5a) (hereafter I6G) structure and its predecessors have in practice been informed only to a small extent by ice dynamical considerations and simulations. Most notably, ice thickness history from the Gr.B simulation of

Tarasov and Peltier [2002, 2003] (hereafter TP02, TP03, etc.) has constituted the GIA reconstruction of Greenland glaciation since publication of the ICE-5G (VM2) model. To the extent that I6G is derivative of ice sheet model results, it is tautologically consistent with the dynamical constraints that these models impose upon possible ice thickness histories. Since the reconstruction of ice thickness history variations from all other regions has continued to rely upon manual tuning, however, it has come to be an issue as to whether ice sheet reconstructions based upon the pure GIA methodology are globally consistent with our increasingly detailed understanding of the physics of ice sheets. Consistency cannot simply be defined in terms of consistency with observations because reconstructions may be nonunique, with the true alternative to I6G potentially depending, for instance, upon deviations of the Earth's viscosity from the simple assumption of radial symmetry [e.g., *van der Wal et al.*, 2015]. If the assumptions of I6G could convincingly be shown to be *inconsistent* with ice sheet physics, then we would have grounds to pursue more elaborate hypotheses about mantle viscosity distribution and past ice cover. In presenting I6G as the observationally validated and currently best approximation to truth, we define consistency in accordance with Ockham's razor by placing the onus upon competing ice sheet coupled GIA models to prove inconsistency.

In a recent ice-sheet-coupled GIA modeling study of Antarctica, *Whitehouse et al.* [2012] locally fit GIA-related observations by assuming an upper mantle viscosity significantly higher than that in I6G and correspondingly predicted a significantly more modest deglacial mass loss since last glacial maximum (LGM). The quality of fits achieved by these authors was lower than that of I6G, but a local simulation of Antarctica in isolation could not logically establish inconsistency with I6G even if the fits were comparable. Grounds for a claim of inconsistency could be established only by fitting the global observational database to equivalently tuned simulations of all major continental ice sheets within the constraints of the pure GIA-based methodology. A global view of the consistency of pre-I6G GIA-based reconstructions of the Laurentide, Fennoscandian, and Greenland ice sheets with the results of the Glacial Systems Model (GSM) was provided in an earlier series of papers by *Tarasov and Peltier* [1997, 1999, 2000, 2002, 2003, 2004]. The shallow-ice approximation-based (SIA-based) model of TP*yy* was trained to fit the GIA constraints by application of a Bayesian inversion process in which GSM parameters were varied randomly through prior assumed ranges of plausibility in a Monte Carlo approach to the solution of the inverse problem of ice sheet reconstruction. While revealing the plausible ranges of solutions for local ice sheets through application of comparable tuning principles, these analyses relied upon a GSM formulation that was insufficiently rigorous to ascribe inconsistencies to GIA-based reconstructions (as opposed to ascribing them to its own extremely ill-constrained initial assumptions). The Gr.B Greenland simulation was incorporated into subsequent GIA-based models because it happened to improve fits to coastal relative sea level histories subject to the simplest constraints, while the Laurentide and Fennoscandian simulations produced poorer fits that could easily be explained without the invocation of more elaborate GIA constraints.

Although extensive efforts by many investigators have considerably improved upon the physical parameterizations and numerical technologies supporting early versions of the GSM, modern ice sheet models such as the Parallel Ice Sheet Model (PISM) [*Winkelmann et al.*, 2011] continue to be characterized by the same essential logical shortcomings. In the PISM model SIA-based dynamics are coupled to shelfy-stream-approximation-based (SSA-based) dynamics [*MacAyeal*, 1989] in order to somewhat improve the representations of glacial till-related processes, floating ice shelves, and iceberg calving, but ice sheet simulations over paleoclimate timescales continue to be highly diffusive and dependent upon gross approximations of the Full Stokes (FS) equations [e.g., *Pattyn et al.*, 2008]. They must therefore still be considered as a somewhat questionable basis for evaluating the physicality of structures near the ice margins and grounding lines of GIA-based reconstructions. Even more significant, however, are the gross approximations that models like PISM continue to invoke for the boundary conditions (BCs) constraining ice sheet dynamics in three critical regions; i.e., (1) at the upper surfaces where ice sheets are exposed to the atmosphere; (2) at the lower surface of the grounded ice sheet (the bed) where sliding may occur; and (3) at the lower surfaces where floating ice shelves are exposed to the ocean, especially close to the grounding line. It is unclear to what degree even the latest generation of paleoclimate timescale ice sheet models would be able to expose physical inconsistencies in I6G, and this is the very important research topic that we report upon herein. We will be employing a new, state-of-the-art suite of numerical methods that combines custom-built applications with public domain community models (including PISM) and that we loosely refer to as the University of Toronto GSM (UofT GSM).

With regard to changes in the upper surface boundary conditions on those ice sheets that continue to exist following the end of the most recent Late Quaternary glacial cycle (i.e., on Greenland and Antarctica), it has

long been standard practice to adjust mean surface temperatures as well as precipitation history and associated positive-degree day (PDD) ablation schemes based upon the measured vertical deposition patterns of $\delta^{18}O$ isotopic evidence from ice cores in order to approximate net mass balance histories [*Ritz et al.*, 1996]. This approach makes dynamical ice sheet modeling possible and may be extended to extinct structures such as the former Laurentide and Fennoscandian ice sheets if the isotopic time series is used to interpolate between the modern and LGM solutions of a full climate model [*Marshall et al.*, 2000]. Its assumptions are, however, extremely tenuous and poorly constrained. Recent modeling work has also introduced parameterizations aiming to represent the significant feedback which is expected to couple ocean climate change to the lower boundary conditions of Antarctic ice shelves [e.g., *Pollard and DeConto*, 2009; *Joughin et al.*, 2014; *Golledge et al.*, 2014]. The results of such preliminary analyses highlight *possible* physical mechanisms of ice-ocean interaction, but depend upon initial assumptions that are even less well constrained than assumptions concerning ice-sheet-atmosphere interaction. In specifying the assumed functional forms of ice sheet mass balances associated with upper and lower surface BCs, prior studies have made no attempt to make use of the GIA constraints that indirectly apply to the mass balance by constraining ice thickness history. The physical adequacy of GIA constraints is not meaningfully tested when ice sheet analysts attempt to fit them by tuning discrete parameters after making gross leading-order assumptions about the geographical structure of mass sources and sinks.

In the present work our goal is to address the issue of poorly constrained ice sheet model mass balances in a way that simultaneously addresses the issue of consistency with I6G. Regarding the GIA-based reconstruction as a coarse-grained, observationally consistent approximation of ice thickness, we can introduce its information into typical ice sheet dynamical simulations through a data assimilation procedure [e.g., *Tardif et al.*, 2014]. Data assimilation is widely used to incorporate observations into atmosphere-ocean forecasts, and the adjustment of mass balance in order to assess ice sheet dynamical consistency with I6G can be straightforwardly achieved if we apply the simple technique of nudging to the ice thickness field [e.g., *Salameh et al.*, 2010]. Taking the PISM ice sheet dynamical system and the SeaRISE modeling protocols as a base solution [*Bindschadler et al.*, 2013; *Nowicki et al.*, 2013a, 2013b], we nudge simulations of Greenland and Antarctica toward I6G and consider the local convergence and mass balance adjustments as nudging timescale decreases toward zero (i.e., toward the limit in which ice thickness history is forced into exact conformity with the GIA-based reconstruction). The objective is to assess whether the latest ice sheet dynamical models suggest any grounds for inconsistency in I6G. Bayesian or other techniques could be used to optimize nudging timescale in tandem with other model parameters, but such technical complexity is not needed to make the point of the current study. Our theoretical approach is developed in detail in section 2, and the UofT GSM numerical structure will be discussed in section 3. Section 4, in what follows, describes our results and the implications of these results concerning the fundamental question concerning the glaciological self-consistency of GIA-based ice sheet glaciation history derived reconstructions. Concluding remarks are offered in section 5.

2. Theory

2.1. Leading Order Considerations

In the analyses to follow we will represent glaciation history in terms of a field, $I(\Omega, t)$, that represents the thickness of a hypothetical ice column at arbitrary geographical position Ω and time t, and will begin by considering the physical and observational constraints to which I is subject. Direct measurements of $I(\Omega, 0)$ and $\frac{\partial I}{\partial t}(\Omega, 0)$ are being made with increasing accuracy at present ($t = 0$), but most evidence of past glaciation patterns for $t < 0$ are indirect and related to relative sea level (RSL) history, say $S(\Omega, t)$. RSL is determined by the following gravitationally self-consistent SLE, i.e.,

$$S(\Omega,t) = C(\Omega,t)\left[\int_{-\infty}^{t}\int \mathrm{d}t' \int_{\Omega} \mathrm{d}\Omega' \left\{L(\Omega',t')\Gamma^{S,L}(\Omega,\Omega',t-t') + T(\Omega',t')\Gamma^{S,T}(\Omega,\Omega',t-t')\right\} + \frac{\Delta\Phi(t)}{g}\right], \quad (1)$$

in which $C(\Omega, t)$ is an ocean function that is equal to unity over the temporally evolving surface area of the global ocean and 0 elsewhere, and $\Delta\Phi(t)$ follows the time variation of the world ocean's gravitational equipotential and is required in (1) to ensure that there is a precise correspondence between the mass of grounded continental ice melted at time t and that which enters the global ocean. $\Gamma^{S,\bullet}(\Omega, \Omega', t - t')$ are the viscoelastic Green's functions for S in terms of the surface mass load per unit area, $L(\Omega, t)$, and the centrifugal

potential load, $T(\Omega, t)$ [e.g., see *Peltier*, 2004; *Peltier and Luthcke*, 2009; *Peltier et al.*, 2015, for discussion]. The latter two source fields are determined by their definitions, respectively:

$$L(\Omega, t) = \rho_i I(\Omega, t) + \rho_w S(\Omega, t)$$
$$T(\Omega, t) = \Omega_0 a^2 \left\{ \frac{2\omega_3(t)}{3} \left[Y_{00}(\Omega) - \frac{Y_{20}(\Omega)}{\sqrt{5}} \right] + \sqrt{\frac{2}{15}} \left[\omega_1(t) - i\omega_2(t) \right] \left[Y_{21}(\Omega) - iY_{2-1}(\Omega) \right] \right\}, \quad (2)$$

in which ρ_i and ρ_w are the respective densities of ice and (fresh) water, a is the mean radius of the Earth, $Y_{lm}(\Omega)$ are the spherical harmonics of degree and order (l, m), and

$$(\omega_1(t), \omega_2(t), \omega_3(t)) \approx (0, 0, \Omega_0)$$

is the time-varying pseudovector that represents variations in Earth's rotational state. The scalar time series $\omega_i(t)$ are deduced by applying global angular momentum conservation as an integral constraint upon the SLE (1) [*Wu and Peltier*, 1984; *Peltier and Luthcke*, 2009; *Peltier et al.*, 2012], in which $\Delta\Phi(t)$ is analogously determined by applying global mass conservation expressed in terms of the following constraint; i.e.,

$$\frac{\mathrm{d}}{\mathrm{d}t} \int \int_{\Omega} L(\Omega, t) \mathrm{d}\Omega = 0. \quad (3)$$

The solution of the integral equation (1) subject to (2) and (3) is a highly nontrivial problem, not only because it is a Fredholm integral equation of the second kind but also because the numerical methodology depends upon the time evolution of the coastline defined by C [*Peltier*, 1994] and upon the grounding of the ice thickness I in regions in which it is in contact with the sea. Assuming that a solution for S in terms of I can be obtained, convolution of L and T with additional viscoelastic Green's functions will yield other GIA-related fields by the following template; i.e.,

$$\Upsilon(\Omega, t) = \int_{-\infty}^{t} \int \int_{\Omega} \left[L(\Omega', t') \Gamma^{\Upsilon, L}(\Omega, \Omega', t - t') + T(\Omega', t') \Gamma^{\Upsilon, T}(\Omega, \Omega', t - t') \right] \mathrm{d}\Omega' \mathrm{d}t', \quad (4)$$

in which the two cases most important for the present study identify $\Upsilon(\Omega, t)$ with the Earth's surface radial displacement, $R(\Omega, t)$, and geoid, $G(\Omega, t)$. To determine the ocean function, $C(\Omega, t)$, in the absence of an ice history (i.e., for $I = 0$), we would consider the sign of the relative displacement,

$$B(\Omega, t) \equiv R(\Omega, t) - G(\Omega, t),$$

of the solid surface with respect to the sea level defined gravitational equipotential surface, noting that $B = -S$ in ocean regions where $C = 1$, that $B = 0$ at the time-dependent coastline, and that $B > 0$ on exposed land where $C = 0$. To determine the ith estimate of the ocean function, $C^{(i)}$, in an ice-free context, an iterative procedure would determine $B^{(i)}$ using appropriate choices of Green's function in equation (4) after the SLE (1) has been solved using the $i - 1^{\mathrm{st}}$ estimate, $C^{(i-1)}$, of the ocean function (which is simply the modern ocean function, $C^{(0)}(\Omega, t) \approx C(\Omega, 0)$ in the initial iteration). The methodology of *Peltier* [1994] applies to the more general case in which there is an ice history (i.e., $I \geq 0$), by making use of an approximation that we will clarify below.

For purposes of computing C in an SLE solution with grounded continental ice, land is effectively the region where *grounded* ice determines the surface mass loading term, $L = \rho_i I$, while ocean is effectively the complementary region where the load term, $L = \rho_w S$, is determined by relative sea level. To clarify the geometry of ice sheet grounding and provide a reference for subsequent mathematical discussion, Figure 1 shows a schematic local geometry in which the geoid is associated with the vertical coordinate isosurface $z = 0$. Archimedes' principle may be employed to determine how coastlines are effectively modified by ice grounded below sea level, and we obtain the following expression for the lower boundary, B_i, of a potentially floating ice column with thickness I and surface elevation $H = B_i + I$ relative to sea level; i.e.,

$$B_i(\Omega, t) = \begin{cases} -\frac{\rho_i I(\Omega, t)}{\rho_w} & \text{for floating ice where } B_*(\Omega, t) < 0 \\ B(\Omega, t) & \text{for grounded ice where } B_*(\Omega, t) \geq 0, \end{cases} \quad (5)$$

in which the grounding line is determined by the zero level not of the sea-level-relative topography, B, but, rather, of the following indicator function, i.e.,

$$B_*(\Omega, t) \equiv B(\Omega, t) + \frac{\rho_i I(\Omega, t)}{\rho_w}. \quad (6)$$

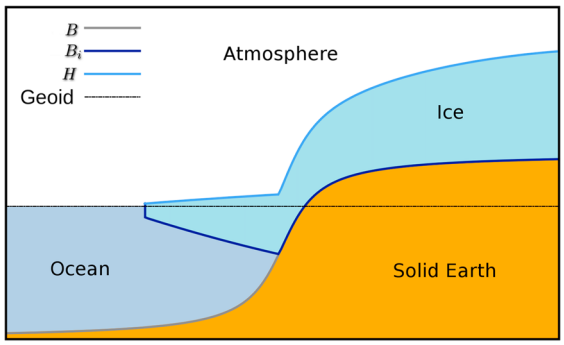

Figure 1. Schematic layout of the geometry of sea level, grounded ice, grounding lines, and floating ice shelves.

Even though the early analyzes of *Peltier* [1994] [see also *Peltier and Fairbanks*, 2006] did not explicitly refer to grounding lines, the heuristic methodology implicitly simplified the iterative SLE algorithm by approximating this function in the following way, i.e.,

$$B_*(\Omega, t) \approx B(\Omega, 0) + S(\Omega, 0) - S(\Omega, t) + I(\Omega, t), \tag{7}$$

where B_* [*Peltier*, 1994, PT in equation (6)] is called the true paleotopography. In local dynamical ice models that evolve the lower surface while neglecting the fact that the $z = 0$ isosurface follows the position- and time-dependent geoid, the following alternative approximation is invoked for B_*, i.e.,

$$B_*(\Omega, t) \approx B(\Omega, t) + \langle S \rangle(0) - \langle S \rangle(t) + \frac{\rho_i I(\Omega, t)}{\rho_w}, \tag{8}$$

in which the scalar function $\langle S \rangle(t)$ reflects the time variation of some suitable local average sea level (which would become eustatic sea level if the whole ocean were used for averaging purposes).

Solution of the SLE (1) for S serves to translate relatively abundant observational constraints on the output fields into constraints upon the input ice thickness history, $I(\Omega, t)$, and upon the radial viscosity and elastic parameter profiles that determine all of the various viscoelastic Green's functions, $\Gamma^{\bigcirc}(\Omega, \Omega', t - t')$. The ICE6_C form of I and the VM5a form of $\Gamma^{\bigcirc}$ can be understood as the outgrowths of a notional inverse method that iteratively selects provisional hypotheses based upon fidelity to the data, i.e.,

$$\begin{aligned} I_{(i+1)} &= \mathbf{I}\left\{ I_{(i)}, \Gamma^{\bigcirc}_{(i)}, S_{\text{obs}} \right\} \\ \Gamma^{\bigcirc}_{(i+1)} &= \mathbf{G}\left\{ I_{(i)}, \Gamma^{\bigcirc}_{(i)}, S_{\text{obs}} \right\}. \end{aligned} \tag{9}$$

The implicit procedures **I** and **G** have in practice involved the adaptation of semiempirical techniques to an ever-expanding array of available data.

2.2. Ice Dynamical Modeling

The pure GIA methodology does not rigorously constrain time dependence of ice thickness, I, with any general hypotheses regarding the physics of ice sheet dynamical evolution. Regardless of its level of sophistication and glaciological consistency, any ice sheet model amounts to the determination of the horizontal flux, **Q**, and the source term, G, in the following local conservation law for I, i.e.,

$$\frac{\partial I}{\partial t} + \nabla_h \cdot \mathbf{Q} = G. \tag{10}$$

Q in equation (10) depends primarily upon the assumptions that a model makes about ice physics, while G depends primarily upon the assumptions that it makes about the climatological and basal processes driving ice ablation and accumulation. Both ice physics and climatological source terms are very heavily approximated in all currently available ice sheet models for paleoclimatological applications, and the introduction of parameters that tune **Q** and G in equation (10) will not automatically yield a better approximation to the truth than the direct parameterization of the glacial history, I, itself. The pure GIA-based approach is clearly underconstrained in the sense that it admits dynamically inconsistent ice histories, but weak, overconstrained $\mathbf{Q} - G$ approximations may just as problematically *suppress* I solutions that would be dynamically consistent with a better approximation. Bayesian techniques apply to the discrete parameter spaces associated with given constraints but clearly cannot address the validity of the constraints themselves.

Granting that modestly tuned and interpreted model results may illustrate the *potential feasibility* of detailed physical mechanisms corresponding to various choices of **Q** and G as well as making predictions that

cannot be derived through pure GIA methods, we can introduce generic ice modeling into the observationally constrained paradigm by formulating equations (2.1) and (10) as follows, i.e.,

$$\begin{aligned} G_{(i+1)} &= G^I\left\{G_{(i)}, \mathbf{Q}_{(i)}, \Gamma^{\bigcirc}_{(i)}, S_{\text{obs}}\right\} \\ \mathbf{Q}_{(i+1)} &= \mathbf{Q}^I\left\{G_{(i)}, \mathbf{Q}_{(i)}, \Gamma^{\bigcirc}_{(i)}, S_{\text{obs}}\right\} \\ \Gamma^{\bigcirc}_{(i+1)} &= \mathbf{G}^I\left\{G_{(i)}, \mathbf{Q}_{(i)}, \Gamma^{\bigcirc}_{(i)}, S_{\text{obs}}\right\} \\ \frac{\partial I_{(i+1)}}{\partial t} + \nabla_h \cdot \mathbf{Q}_{(i+1)} &= G_{(i+1)} + \Delta G_{(i+1)}, \end{aligned} \tag{11}$$

in which $\Delta G_{(i+1)}$ represents a term that dynamically nudges the $i + 1^{\text{st}}$ approximation of the ice thickness history toward the ith approximation. Nudging is a well-established approach in multiscale AO modeling [e.g., *Salameh et al.*, 2010], in which the relaxation term keeps local high-resolution simulations consistent with larger-scale low-resolution simulations. Even if the coarse-grained ice thickness solution $I_{(i)}$ has been fit to observations by means other than continuum-mechanical modeling, it can be used to nudge the succeeding solution, $I_{(i+1)}$, by adding a nonlinear exponential relaxation term with timescale τ_f to the mass balance, i.e.,

$$\Delta G_{(i+1)} = -\frac{I_{(i+1)} - I_{(i)}}{\tau_f}. \tag{12}$$

The "glaciological consistency" and uniqueness of $I_{(i)}$ can be evaluated a posteriori, with respect to a particular choice of ice model and τ_f, through comparisons of $\Delta G_{(i+1)}$ with $\nabla_h \cdot \mathbf{Q}_{(i+1)}$, and G_i. For grounded ice regions, it is well known that ice flux in the simplest isothermal shallow ice models takes the form

$$\mathbf{Q} \approx -D(H, \|\nabla_h H\|, \ldots)\nabla_h H,$$

giving rise to the following evolution equation, i.e.,

$$\frac{\partial I}{\partial t} = \frac{\partial}{\partial t}\left(H - B_i\right) \approx \frac{\partial H}{\partial t} = \nabla_h \cdot \left[D(H, \|\nabla_h H\|, \ldots)\nabla_h H\right] + G + \Delta G, \tag{13}$$

and this allows us to talk about the ice elevation field, $H = B_i + I$, of the I6G solution as being diffusively "smoothed" by ice dynamics that approximate a diffusion equation in which diffusivity, D, depends nonlinearly upon H and its 2-D gradient on the surface of the sphere [e.g., *Bueler et al.*, 2007]. Taking into account 1-D matched asymptotic analyzes of normal ice flux at the grounding line [*Schoof*, 2007a, 2007b], this generic nonlinear diffusion equation can be generically matched to a nonlinear Robin-type boundary condition, i.e.,

$$\mathbf{Q} \cdot \frac{\nabla_h B_*}{\left|\nabla_h B_*\right|} \approx C I^c = C\,(H - B)^c \quad \text{where} \quad B_* = 0, \tag{14}$$

in which C and c are phenomenological constants. Equation (14) is most significant for its implication that an ice sheet will collapse if the retreat of the grounding line increases the outward grounding line flux by exposing a larger thickness of ice (as happens if B decreases in the direction of retreat).

Modern ice models like PISM [*Winkelmann et al.*, 2011] add many layers of sophistication to the schematic leading-order problem of equations (13) and (14), but the theoretical principles of this subsection apply regardless of the details of the ice model. In the following subsections, we will discuss the smoothing and climatological mechanisms that have been built into the PISM model, most of which are the same as were initially built into the previous versions of the UofT GSM of *Tarasov and Peltier* [1997, 1999, 2000, 2002, 2003, 2004]. We choose to employ PISM as the ice sheet dynamical core in the analyses to follow rather than the previous version of the UofT GSM in spite of their similarities because PISM has been efficiently parallelized.

2.3. PISM Model Coupling and BCs

The generic three-dimensional thermomechanical ice model couples to the framework of the previous subsection through the following prescriptions of ice flux and surface mass balance, i.e.,

$$\begin{aligned} \mathbf{Q}(\Omega, t) &= \int_{z=B_i}^{H} \mathbf{u}\,(\Omega, z, t)\,\mathrm{d}z, \\ G(\Omega, t) &= G_s(\Omega, t) + G_b(\Omega, t) \end{aligned} \tag{15}$$

in which $\mathbf{u}(\Omega, z, t)$ is the three-dimensional ice velocity vector inside the ice volume, and in which $G_s(\Omega, t)$ and $G_b(\Omega, t)$ are the respective parameterizations of surface and basal mass balance. Some further details about the particular PISM framework for determining the fields in the RHS of equations (2.3) are reviewed in Appendix A. Adjustments of the modern surface mass balance, $G_s(\Omega, 0)$, for paleoclimate change generically build upon the following formula for determining local surface temperature change, $\Delta T(\Omega, t)$, in terms of variations in simulated glacial elevation, $H(\Omega, t)$, and measured ^{18}O concentrations, $\delta^{18}\mathrm{O}(t)$:

$$\Delta T(\Omega, t) = -\lambda_T \left[H(\Omega, t) - H(\Omega, 0)\right] + \alpha_c^{-1} \left[\delta^{18}\mathrm{O}(t) - \delta^{18}\mathrm{O}(0)\right] \tag{16}$$

in which λ_T is the temperature lapse rate, and α_c is an empirical constant relating globally constant temperature deviation to the δ^{18}O time series derived from a nearby ice core. Ice-core-based climate BC adjustments in the newest models remain essentially identical to those employed in the initial version of the UofT GSM (TP02, etc.) and other methodologies of the same approximate vintage. By compounding a succession of ad hoc assumptions, such parameterizations constitute a weak logical link in the traditional paleoclimate ice modeling paradigm. Parameterizations of the basal mass balance, G_b, are even less standardized in the literature than those of G_s, and our introduction of the nudging mass balance, ΔG, beneficially imposes observationally grounded adjustments upon the poorly constrained climatological mass balance, $G = G_s + G_b$. At the idealized level at which ice sheet dynamical models explicitly parameterize their physics, ΔG is interpretable simply as a perturbation of the net mass balance from surface and basal contributions. In order to prevent negative ice thicknesses, represent calving, and enforce other numerical constraints, however, "practical" ice sheet models also introduce additional heuristics that make it difficult to precisely interpret their implicitly specified G. In tandem with Appendix A, this subsection addresses the general theoretical issues with reference to PISM.

From the preceding, we can see how our "nudging" approach conceptually relates to, and improves upon, the standard use of observations in paleoclimate BCs. If we imagined that ΔG could only represent an adjustment to surface precipitation and ablation, then we could place a lower bound on the order of magnitude of τ_f simply by reasoning that the atmosphere could not transfer enough energy to induce catastrophic surface accumulation or ablation at a rate greater than about $\mathcal{O}$(1 m/yr) (the modern extremes of annual mass balance in the vicinities of Greenland and Antarctica). Since ice sheet thickness is $\mathcal{O}$(1000 m), we get $\tau_{f\,\mathrm{min}} \approx 1000$ years. This physical lower bound on τ_f ceases to be relevant when we note that the mass balance nudging term, ΔG, includes not only contributions from G_s but also contributions from iceberg calving and from basal processes in both grounded and shelf ice and related feedbacks. The modern extremes in the relevant mass balances are highly uncertain but known to be much larger than their surface analogues, and the envelope might well have been pushed much further by past climate catastrophes (e.g., those associated with the meltwater pulses that occurred during the most recent glacial interglacial transition upon which we will focus in what follows). Noting that a typical paleoclimate timescale ice dynamical model with an $\mathcal{O}$(1 year) time step would show no deviation from $I_{(i)}$ if τ_f were comparable, we can set a practical lower bound of $\mathcal{O}$(10 years) on the nudging timescale.

Concerning the ice dynamical representation of ice shelf calving, older ice models such as the version of the UofT GSM employed in TP02 adhered to the formulation in which ice thickness, $I \geq \varepsilon$, has at least some infinitesimal value (say, $\varepsilon = 1$ m) everywhere, and in which G_b implicitly adjusts to enforce the constraint $I = \varepsilon$ where it would otherwise ensue that $I < I_{\mathrm{crit}}$. The minimal thickness, I_{crit}, can straightforwardly assume the value ε for grounded ice, and a simple thickness calving parameterization is obtained if I_{crit} assumes a larger value (typically in the range 50–250 m) for floating ice shelves. While continuing to accommodate the thickness calving mechanism, newer ice models such as PISM can also represent calving in terms of horizontal kinematic boundary conditions. Since kinematic calving introduces a large, indirect effective mass balance into G, and since PISM implements it only in a semirigorous, grid-dependent manner, we will conclude this subsection with a mathematically precise formulation of the theoretical principle.

In the vertical direction, the ice conservation equation (10) derives from a kinematic BC for 3-D velocity, $\mathbf{u}(\Omega, z, t)$, which must satisfy the following kinematic constraint at the upper boundary, $z = H = B_i + I$, i.e.,

$$\frac{\partial H}{\partial t} + \mathbf{u}(\Omega, H, t) \cdot \nabla_h H = 0.$$

To set up the corresponding horizontal BC at a calving front curve, Ω_c, we keep in mind the definition of the ocean function, C, and define a 2-D field, C_I, to be 0 where there is no ice, 1 where there is ice, and 1/2 at the

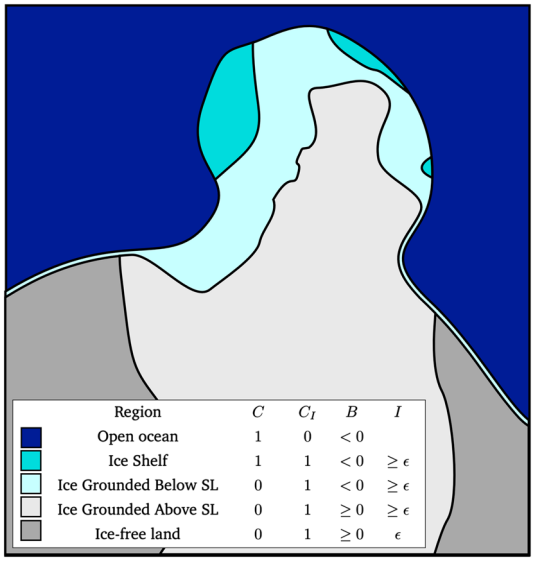

Figure 2. Schematic distribution of the various ice flow regimes: (1) open ocean ($C = 1$, $C_I = 0$); (2) ice shelf ($C = C_I = 1$); (3) ice grounded below sea level ($C = 0$, $C_I = 1$, $B < 0$); (4) ice grounded above sea level ($C = 0$, $C_I = 1$, $B \geq 0$); and, (5) ice free land ($C = 0$, $C_I = 1$, $B \geq 0$, $I = \varepsilon$).

notional edge of the ice (i.e., along the curve Ω_c). Figure 2 schematically depicts the horizontal distribution of dynamical regimes, with a legend that indicates the values of the various fields. It is straightforward to show that the scaled ice thickness $C_I I$ will satisfy a simply scaled conservation law,

$$\frac{\partial}{\partial t}\left(C_I I\right) = -\nabla_h \cdot \left(C_I \mathbf{Q}\right) + C_I\left(G + \Delta G\right), \quad (17)$$

if C_I is advected by a velocity $\mathbf{Q}/I$, i.e., if

$$\frac{\partial C_I}{\partial t} = -\left(\frac{\mathbf{Q}}{I}\right) \cdot \nabla_h C_I. \quad (18)$$

A vertically homogeneous horizontal BC on $\mathbf{u}(\Omega_c, z, t)$ results if we interpret $\mathbf{Q}/I$ along Ω_c in the following terms, i.e.,

$$\mathbf{u}(\Omega_c, z, t) + \mathbf{U}_c(\Omega_c, t) = \frac{\mathbf{Q}}{I}(\Omega_c, t), \quad (19)$$

in which $\mathbf{U}_c(\Omega_c, t)$ is an equivalent velocity quantifying mass loss due to iceberg calving. The parameterization of this velocity is reviewed in Appendix A along with other relevant details concerning the PISM model.

3. Numerical Methods

3.1. Ice Sheet Modeling Framework

From the standpoint of numerical methods and their software implementation, the nominal takeoff point for the present study was in the work of TP*yy*, which included the first coupling of an ice sheet dynamical model (the GSM) to GIA-based reconstruction techniques that solved the SLE in spectral space. It has been a long-standing goal of the broader research community, including ourselves, to investigate and improve upon the technical aspects of such analyses, and the current, updated version of the UofT GSM reflects a metamodeling strategy that combines a variety of open source codes with a suite of in-house software that deals with interfacing, data handling and postprocessing, and coupling to the SLE solver. Because of its efficiently parallelized numerical structure, the PISM model is, as noted in section 1, invoked for paleoclimate timescale analyses like the ones that we will describe herein. Efficiency is maintained through the employment of low-order SIA-SSA physics and structured grids in long integrations with relatively coarse and uniform spatial resolution. The UofT GSM framework also accommodates the structure of the Ice Sheet System Model (ISSM), which was developed at NASA's Jet Propulsion Laboratory [*Larour et al.*, 2012], and which allows for simulations based upon higher-order Full Stokes (FS) physics and upon the Blatter-Pattyn approximation [*Blatter*, 1995; *Pattyn*, 2003] to be carried out using unstructured grids with unlimited capacity for local resolution enhancement in regions of interest. ISSM-based analyses will not be considered in the present work because the underlying computational techniques are not sufficiently efficient to support simulation lengths beyond the century timescale.

Techniques for formulating and tuning long-term simulations of isolated ice sheets have been extensively discussed in the above cited literature and elsewhere, and the crucial issue, for purposes of the present study, is the need to maintain consistency in the global enforcement of simple GIA constraints. In the absence of such consistency, it is difficult to logically address the arguments that other investigators have begun to make based upon coupled GIA ice sheet models of Antarctica [e.g., *Whitehouse et al.*, 2012; *Gomez et al.*, 2012; *Rovere et al.*, 2014]. BCs describing phenomena associated with geothermal heat flux and ice-core-inferred surface climate variability are, of course, clearly tied to measured local conditions where the appropriate data are available, but the credibility of models suffers in the manner discussed in section 1 if local tunability is extended to all phenomenology that is not directly constrained by observations (e.g., ice calving, ice hardness, mantle viscosity, etc.). The application of Bayesian techniques enforced a kind of global consistency upon many

of the local ice sheet simulations of TP*yy* by determining an equivalently defined optimal parameter set for each case, but it is much more convincing to everywhere make the *same* local assumptions about unknown parameters. By introducing I6G as an observationally validated basis for the nudging of ice sheet thickness, we make it possible to study universality in large-scale ice sheet dynamics.

3.2. SLE Solver

The SLE solver supporting I6G and its predecessors is at the time of writing still implemented through legacy FORTRAN code that has yet to be fully updated for the modern, C++-based numerical framework. The essential algorithm entails iteratively solving the SLE (1), starting from the assumption that the modern ocean function has remained constant throughout history, $C_{(0)}(\Omega, t) = C(\Omega, 0)$. This assumption is naturally contradicted when $C_{(0)}(\Omega, t)$ and $I(\Omega, t)$ are used to compute the initial RSL estimate, $S_{(0)}(\Omega, t)$, by integral convolution in spectral space, but the inverse spectral transform of $S_{(0)}(\Omega, t)$ can then be employed along with $I(\Omega, t)$ to compute an improved ocean-ice mask, $C_{(1)}(\Omega, t)$, based, as previously discussed, upon the sign of the grounding indicator function, $B_{*(1)}(\Omega, t)$. The procedure for computing $S_{(i+1)}(\Omega, t)$ and $C_{(i+1)}(\Omega, t)$ in terms of $S_{(i)}(\Omega, t)$ and $C_{(i)}(\Omega, t)$ can be extended ad infinitum, and the results appear to converge to physically consistent solutions (although our overall framework includes mathematical and numerical approximations that would be difficult to rigorously analyze and that therefore remain subject to empirical validations of the kind that we are undertaking in this work). Further details of the sea level theory and numerical methods have been extensively discussed elsewhere [*Peltier*, 2004, 2007; *Peltier et al.*, 2012].

For the purpose of a posteriori validation with respect to RSL-related observations, the full sea level theory is used to compute the RSL impact, $S(\Omega, t)$, of a simulated glacial thickness history, $I(\Omega, t)$. When $I(\Omega, t)$ is nudged toward its I6G form, $I_*(\Omega, t)$, it stands to reason that $S(\Omega, t)$ should correspondingly adjust toward its I6G form, $S_*(\Omega, t)$. Beyond the strong coupling introduced through the nudging term, ΔG, I6G has a dynamical effect on the evolution of I through two additional mechanisms. Sea level change in continental-scale ice simulations is, as mentioned previously, most often represented as the eustatically distributed total ice gain/loss. At dynamical simulation time t, the past I6G RSL history, $S_*(\Omega, t' < t)$, is, in addition, used in tandem with the past simulated ice history, $I(\Omega, t' < t)$, to approximate the dynamical vertical motion, $\partial B/\partial t(\Omega, t)$, of the surface of the solid Earth. This coupling has been fully implemented as an improved alternative to the simple bedrock evolution models that have been provided in the public release of the PISM model.

4. Results and Discussion

4.1. Overview

As discussed above, the principle behind our approach requires that all ice sheet model parameters be common to both Greenland and Antarctica unless direct observations dictate otherwise. To achieve this end, we aim to construct a generic hybrid parameter regime that represents both ice sheets consistently within the SeaRISE modeling protocols [*Bindschadler et al.*, 2013; *Nowicki et al.*, 2013a, 2013b]. These protocols are focused upon the need to provide forecasts of future sea level rise and have implementations that differ somewhat between ice models, but the publicly released version of PISM includes a paleoclimate spin-up procedure based on publicly available software, configuration scripts, and data sets. We cite the PISM SeaRISE models of Greenland and Antarctica as making typical modeling assumptions and apply the same procedure to both ice sheets while nudging the paleoclimate-related ice dynamics to I6G. Results from 100 year simulations with modern boundary conditions are used to initialize 200,000 year simulations in which the final ice thickness is held constant while other ice dynamical fields equilibrate with it (this procedure is very similar to that employed in TP02 in their early analyses of the glaciation history of Greenland). The latter simulations run quickly with no ice surface evolution, and their asymptotic end-states are hypothesized to be generically consistent descriptions of glaciation during epochs when historical paleoclimatology resembled modern climatology. We follow common procedure by placing the initial conditions of paleoclimate simulations with full physics in the Eemian warm period, setting $t_i = -122.5$ kyr B.P. to the time of the first discrete frame in the I6G reconstruction. Relevant fields from simulations are then saved at times that coincide with subsequent "frames" of the reconstruction.

Apart from the information in the I6G reconstruction, local observational inputs to the ice dynamical model are limited to the following data sets: modern ice thickness and basal topography (*Bamber et al.* [2001], for Greenland and *Le Brocq et al.* [2010], for Antarctica); modern surface precipitation and temperature (*Ettema et al.* [2009], for Greenland and *Le Brocq et al.* [2010], for Antarctica); geothermal heat

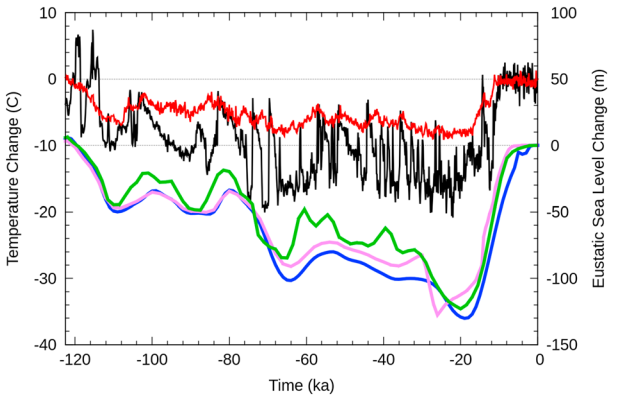

Figure 3. Time series of climatological temperature adjustment, $\Delta T(t)$, inferred from the Greenland GRIP ice core (black) and the Antarctic Vostok ice core (red). The SPECMAP time series of eustatic sea level change is shown (in blue) along with a version corrected for ocean temperature (green) and an estimate based on eustatic sea level equivalent I6G ice volume change (in violet). The *y* scale for sea levels is shown on the right axis.

flux (*Shapiro and Ritzwoller* [2004], for both Greenland and Antarctica); and ice-core-based estimates of climatological surface temperature variations at the GRIP ice core site in Greenland [*Johnsen et al.*, 1997] and at the Vostok ice core site in Antarctica [*Petit et al.*, 2001]. Figure 3 plots the local $\Delta T(t)$ time series for Greenland (in black) and Antarctica (in red), along with the time series for global eustatic sea level change according to the SPECMAP data set [*Imbrie and McIntyre*, 2006], according to SPECMAP corrected for variations in ocean temperature [*Waelbroeck et al.*, 2002], and according to the eustatic sea level history of the I6G model (in blue, green, and violet, respectively). All of these time series are closely related, and the I6G representation is employed to enhance the internal logical consistency of this study. For lack of any more sophisticated and scientifically principled approach, ice sheet modeling protocols have applied point estimates of temperature change over entire ice sheets while uniformly introducing eustatic sea level change at all continent margins. Such assumptions are

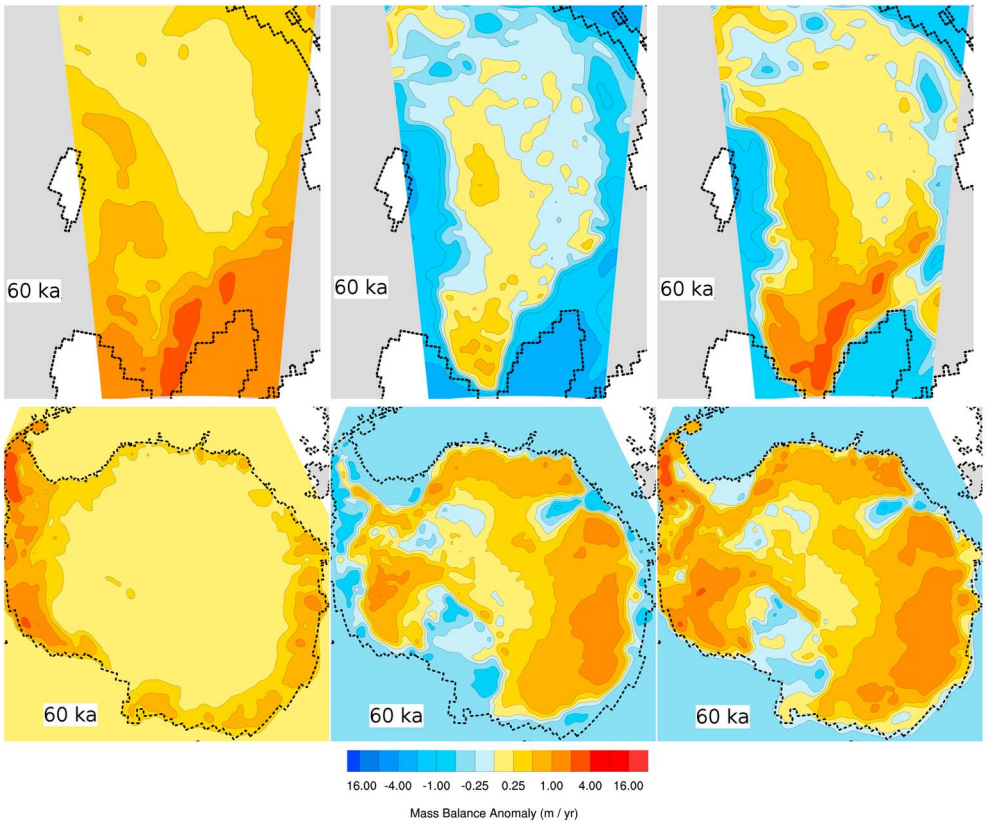

Figure 4. Climatological mass balances on (top row) Greenland and (bottom row) Antarctica plotted for (left column) basic SeaRISE-type assumptions; (middle column) nudging term, ΔG, for relaxation to I6G with $\tau_f = 1000$ years; (right column) total mass balance. Continental margins are represented in this and subsequent figures as dotted 2000 m isobaths.

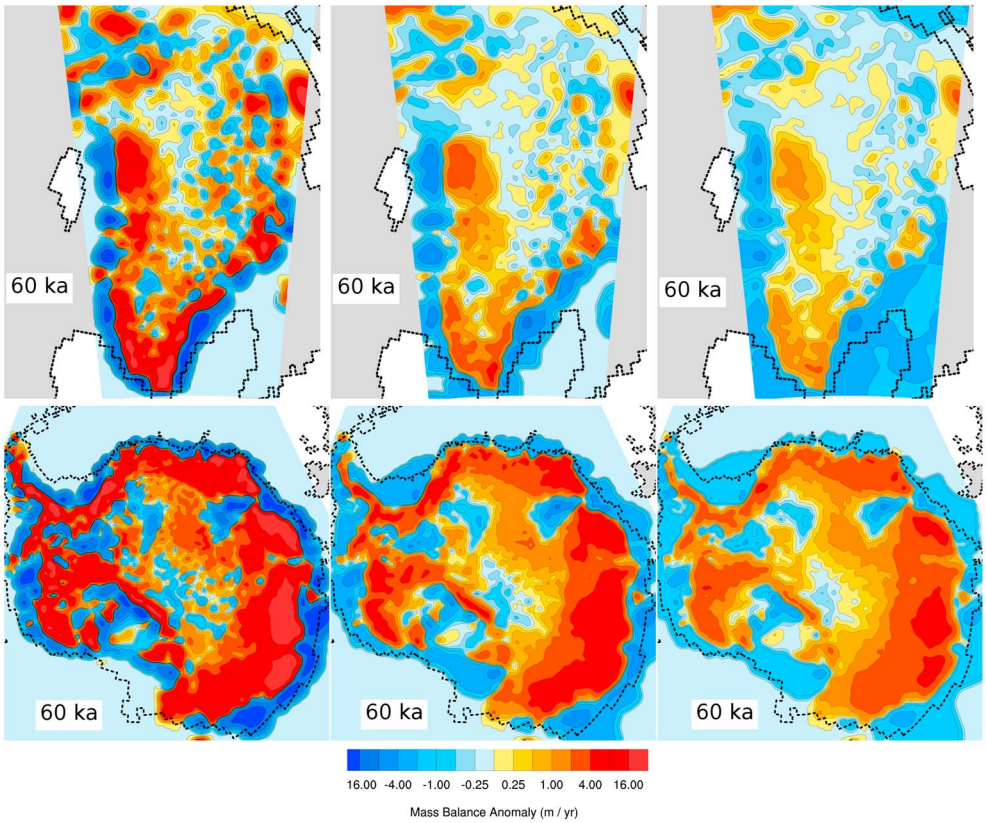

Figure 5. (top row) Greenland and (bottom row) Antarctic mass balances from nudging term, ΔG, for relaxation to I6G with (left column) $\tau_f = 20$ years; (middle column) $\tau_f = 100$ years; and (right column) $\tau_f = 200$ years.

clearly questionable, and our nudging to the data-constrained I6G reconstruction constitutes a suitably local modification of any given assumption concerning net mass balance.

As discussed in section 2.2, the nudging term, ΔG, might be interpretable as a simple correction to the climatological surface mass balance so long as τ_f does not fall below about $\mathcal{O}(1000)$ years. For $\tau_f = 1000$ years nudging applied to both Greenland (top row) and Antarctica (bottom row), Figure 4 juxtaposes contour plots of ΔG (middle column) with the unmodified climatological surface mass balance (left column) and with the total mass balance consisting of the sum of the two (right column). Pertaining to snapshots taken at about the middle of the most recent glacial cycle (60 kyr B.P.), the plots are framed by dotted continental margins (represented by 2000 m deep isobaths) and smoothed by a simple nine-point filter for visual clarity. They show unmodified mass balances involving accumulation that is, for both Greenland and Antarctica, concentrated inhomogeneously along the continental margins while dropping to small levels over interior ice plateaus. The choice of relatively large τ_f keeps the global amplitude of ΔG consistent in both cases with that of the poorly constrained surface accumulation, and anomalous mass balances for Greenland appear in regions where they are interpretable as corrections to significant base accumulation, G. This interpretation becomes problematic for the Antarctic case, however, because the implied ratio of anomalous to unmodified mass balance amplitudes is very large over large regions. This fraction increases and makes ΔG entirely implausible as a correction to surface accumulation and ablation as τ_f decreases below 1000 years. For Greenland (top row) and Antarctica (bottom row), Figure 5 plots the smoothed nudging terms that arise from choices of $\tau_f = 20$ years (left column), $\tau_f = 100$ years (middle column), and $\tau_f = 200$ years (right column). Figures 4 and 5 show that the spatial distributions of weaker Greenland nudging and stronger Antarctic nudging remain very similar for all choices of τ_f but that the mass balance adjustment becomes more intense and more localized about the ice sheet margins as τ_f decreases from 200 years to 20 years.

If ΔG could be interpreted *only* as a correction to surface accumulation and ablation because the ice sheet model was otherwise rigorously constrained by physical understanding, then the results shown in Figures 4 and 5 would be implausible and claims could be made about the inconsistency of I6G. It was made clear

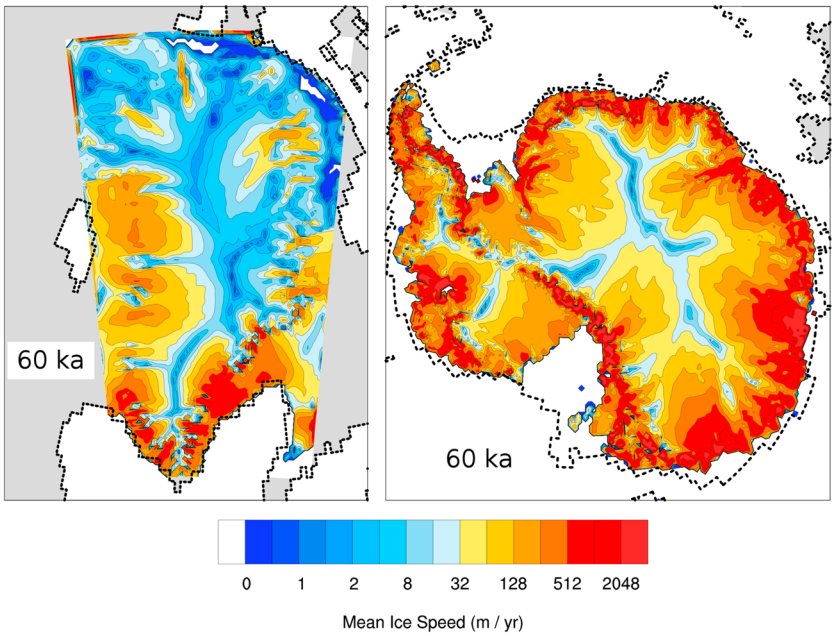

Figure 6. Magnitude of vertically averaged velocity (or, $\|\mathbf{Q}\|/l$) for grounded ice on Greenland and Antarctica at 60 kyr B.P.

in previous discussion, however, that the SIA-SSA approximation and associated physical parameterizations may also inadequately represent truth in regions where solutions depend strongly upon ice streaming and ice sheet margin dynamics or upon the detailed evolution of ice shelves and grounding lines. The spatial patterns in the nudging mass balances in Figures 4 and 5 suggest just such an interpretation, and Figure 6 complements the results from the $\tau_f = 1000$ year case by showing the corresponding vertically averaged ice speeds ($\|\mathbf{Q}\|/l$) for the *grounded* components of the Greenland (left) and Antarctic (right) ice sheets. We can see clear qualitative evidence of ice loss being associated with strong outflow regions (notional ice streams) and with calving at the ice margins. These losses are balanced by enhanced ice accumulation in the western and southern parts of the Greenland ice sheet and in the eastern and western parts of the Antarctic ice sheet. In these regions, strong nudging mass balances, ΔG, and corresponding strong ice flows are interpretable as observationally constrained proxies for phenomenology that could be represented through improvements in the PISM-UofT GSM assumptions. Bayesian or other tuning methods may discover *better* fits within the *present* parameter space (and thereby make an even stronger case for the consistency of I6G), but such techniques cannot substitute for the advancement of detailed physical understanding if the objective, as in the present work, is to investigate potential inconsistencies in I6G.

The physical interpretation of anomalous nudging mass balances is just one of the factors guiding our discussions about consistency between GIA-based and ice sheet dynamical results, and two others relate to consistency with observations and with qualitative glaciological intuition. While depending upon the weakest nudging mass balance adjustment and therefore allowing the greatest degree of smoothing by ice sheet dynamics, the $\tau_f = 1000$ year simulations are problematic in the other two respects. They are outliers in terms of quality of fit to pure GIA constraints, and Figure 6 shows a qualitatively implausible extension of grounded ice flowing far into Baffin Bay and Davis Strait off Western Greenland, as well as into the Greenland and Norwegian Seas off the east coast. The narrower continental shelf around Antarctica does not permit such grounded ice overflows, but most of the ocean-covered domains of both $\tau_f = 1000$ year simulations are implausibly covered by either grounded or floating ice. These results highlight how critically ice sheet structures in unmodified simulations depend upon the parameterization of calving, for which we consistently employ a combination of eigen-calving with constant $K = 3 \times 10^{16}$ m/s and thickness calving below 250 m for both Greenland and Antarctica (the detailed mathematical representation of calving in PISM is reviewed in Appendix A). The six cases illustrated in Figure 5 will be the basis for the following discussions of Greenland (section 4.2) and Antarctica (section 4.3). The most strongly nudged (or, most weakly smoothed) $\tau_f = 20$ year cases will be taken as the reference when a simulation with particular τ_f must be referred to.

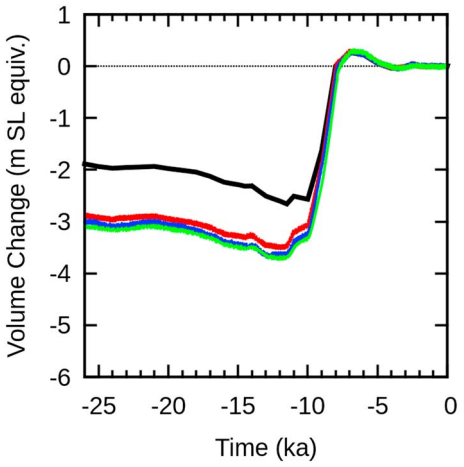

Figure 7. Variations of total Greenland ice volume with respect to modern, expressed as an equivalent sea level change for I6G (black) and for the $\tau_f = 20$ years (red), $\tau_f = 100$ years (blue), and $\tau_f = 200$ years (green) solutions.

4.2. Greenland

The parameterized physics in our PISM-based simulations of Greenland are considerably more complex and rational than the relatively ad hoc techniques that TP02 applied to tuning the Gr.B GSM simulation that became the ICE-5G (VM2) representation of Greenland (and, by inheritance, the I6G representation as well). This increased sophistication apparently makes little difference in the interior of Greenland, where the nudging mass balances, ΔG, depicted in Figure 5 have relatively low amplitude. Since the total variations in Greenland ice volume contribute only minimally to the eustatic sea level variations illustrated in Figure 3, there are in any case few observational constraints that may be applied to constrain the bulk deglaciation of Greenland since LGM. Figure 7 plots the ice volume time series from the three Greenland simulations of Figure 5, as compared to I6G and expressing the deviations from modern ice sheet volumes as equivalent eustatic sea level reductions. As τ_f decreases from 200 years to 20 years, the three new simulations become marginally closer to the 2 m sea level equivalent post-LGM ice loss of the I6G reconstruction for Greenland. This convergence is, however, slow, and simulations nudged at all three timescales consistently generate approximately 1 m in additional sea level rise (i.e., a total of approximately 3 m rather than the 2 m that is characteristic of the loss in I6G). New physics therefore leads to a meaningfully different prediction for

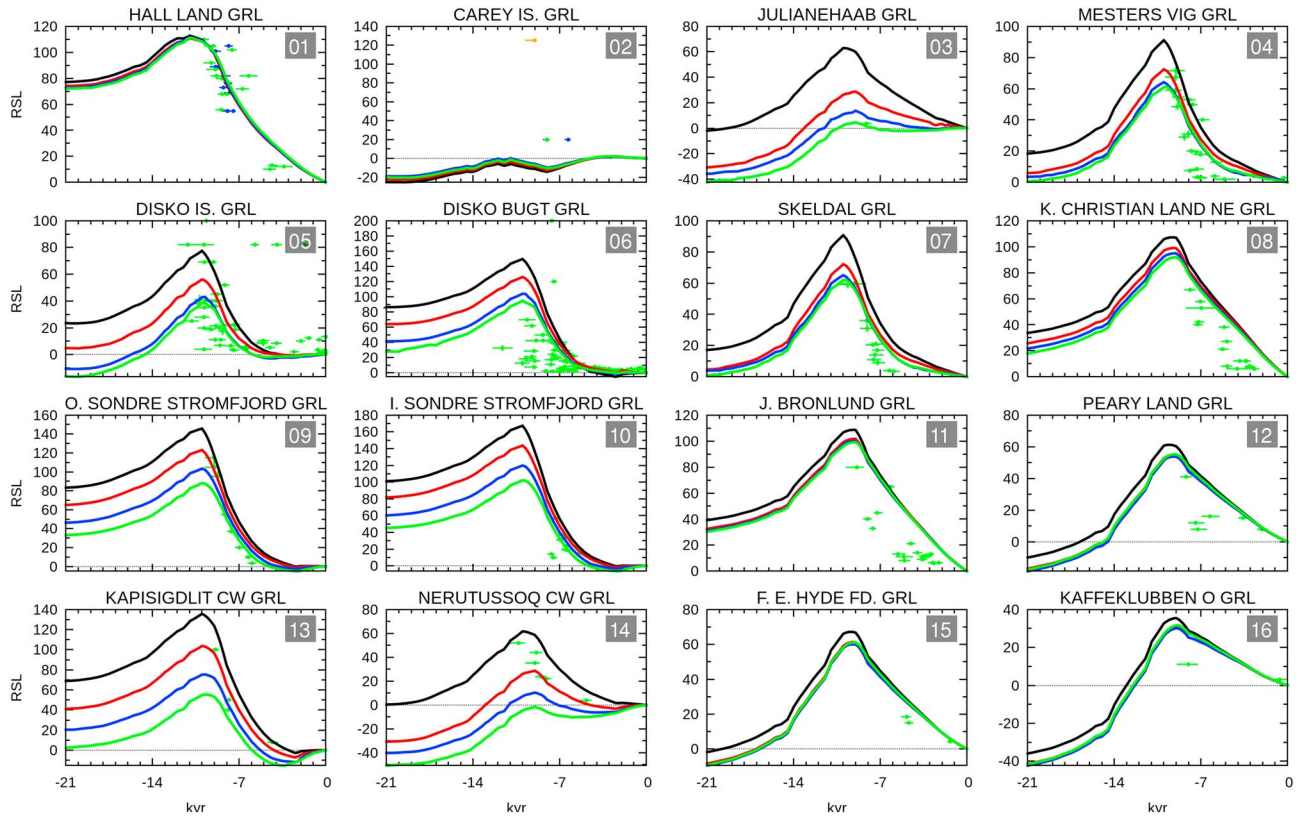

Figure 8. RSL curves from the $\tau_f = 20$ years (red), $\tau_f = 100$ years (blue), and $\tau_f = 200$ years (green) Greenland simulations compared to I6G (black) and overlaid on observational data at the 16 stations discussed in TP02.

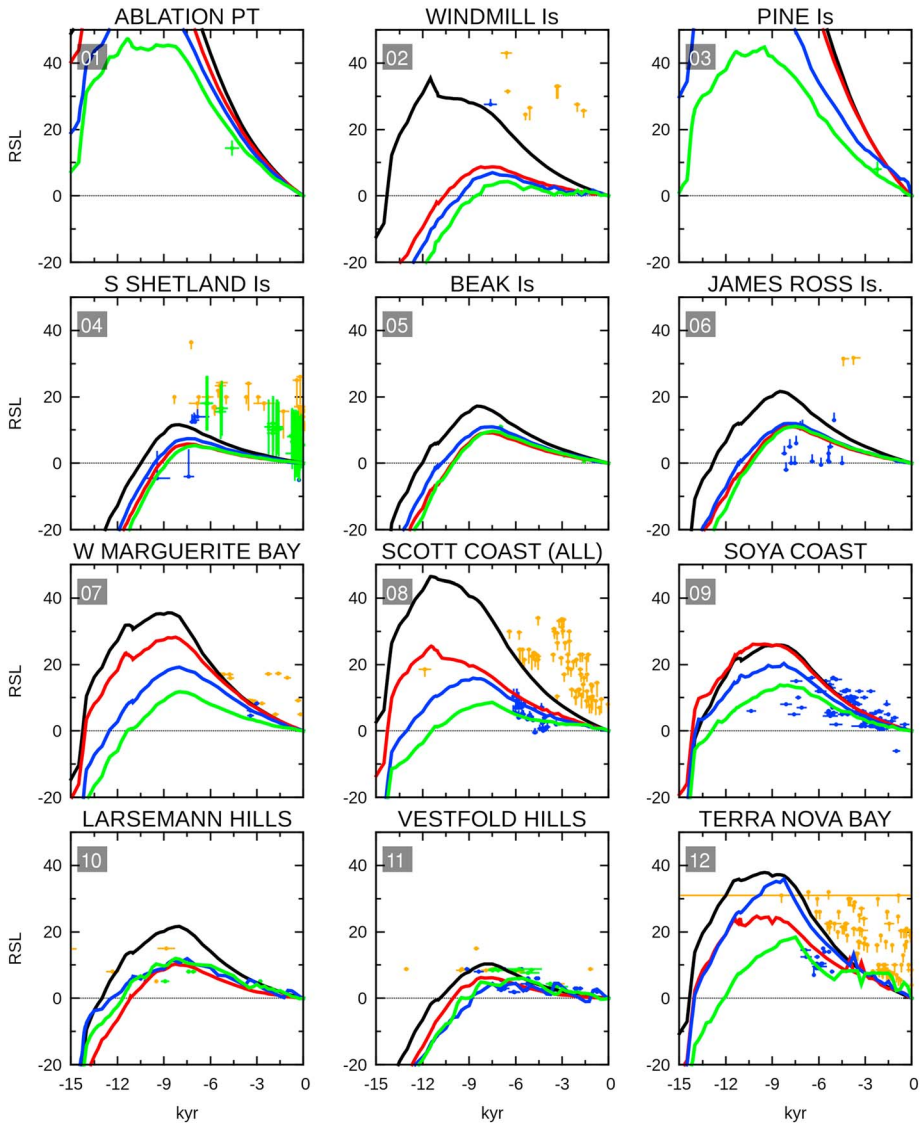

Figure 9. RSL curves from the $\tau_f = 20$ years (red), $\tau_f = 100$ years (blue), and $\tau_f = 200$ years (green) Antarctic simulations compared to I6G (black) and overlaid on observational data at the 12 stations discussed in *Argus et al.* [2014].

total ice volume change, but there are no particular observational grounds on the basis of which this particular discrepancy might be resolved.

The weak convergence of nudged solutions to I6G with decreasing τ_f may be interpreted as a measure of the nonuniqueness in the inferred post LGM glaciation history of Greenland. Insofar as Greenland is concerned, paleoobservations apply mostly to local variations in RSL near coastlines. Figure 8 compares I6G RSL results with those produced by the three nudged simulations for the localities discussed in TP02 in relation to the original tuning of the Gr.B simulation for observational consistency. The RSL curves almost always converge to the I6G fit as τ_f decreases, but the strength of convergence varies from station to station. Evaluated with respect to the often scattered and sparse original observations, weak convergence does suggest a marginally poorer fit at one station (Nerutussoq in the southern tip of Greenland). At the nine or so other stations where convergence is weak, however, RSL curves from partly converged nudged solutions actually provide better fits to the observations, while the envelope generated by varying τ_f quantitatively brackets much of the scatter in the data. The nudged RSL curves at the remainder of the stations exhibit very strong convergence to the corresponding I6G curve.

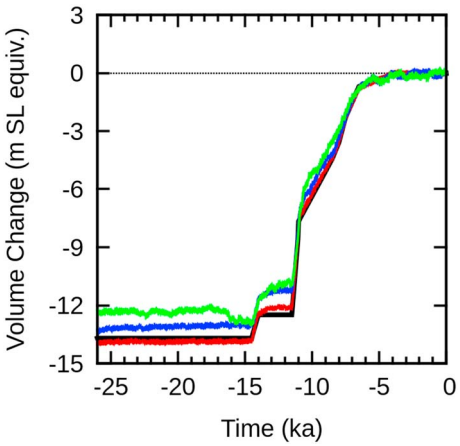

Figure 10. Variations of total Antarctic ice volume with respect to modern, plotted using the same conventions as used in Figure 7 for the Greenland case.

Overall, the new nudged simulations of Greenland provide strong evidence for the physical consistency of the I6G reconstruction while also suggesting a way of bracketing and quantifying observational scatter and solution nonuniqueness. A similar approach will next be applied to the I6G reconstruction of Antarctica, where the detailed ice history derives from direct tuning rather than from the indirect tuning of a previously produced dynamical ice sheet model.

4.3. Antarctica

RSL-based observational constraints have played a much less important role in the I6G reconstruction of Antarctica than in the ICE-5G (VM2) reconstruction for Greenland glaciation history, but *Argus et al.* [2014] do discuss fits to RSL data at 12 stations that we will also analyze. Analogously to Figure 8 for Greenland, Figure 9 compares RSL curves from the three nudged Antarctic simulations with I6G at these 12 stations. The same essential interpretation carries over, and there happens once again to be a single outlier station (at Windmill Island) where nonconvergence to I6G suggests a poorer fit to the observational data. From a broad comparison of the Antarctic RSL fits with their Greenland analogues, we can see that there is much more scatter in the observations and that this is accompanied by more dynamical "noise" in the simulation results. In an unusual departure from the physics exhibited at other stations, the RSL curve from the $\tau_f = 100$ years nudged simulation actually fits I6G better at Terra Nova Bay than the $\tau_f = 20$ years curve. The explanation for such an anomaly must lie in nonlinear ice margin dynamics, but our methodology nevertheless proves its value overall by enabling the scatter and nonuniqueness in fits to be bracketed by variations in τ_f.

Moving on to the total sea level equivalent ice volume change since LGM, Figure 10 compares the nudged Antarctic results with I6G using the same conventions that we used in Figure 7 for Greenland. Although still representing only a fraction of total global sea level change, the I6G estimate for Antarctica (approximately 13.6 m) overwhelms the 2 m − 3 m value for Greenland. The convergence of the nudged deglaciation curves as τ_f decreases from 200 years to 20 years also differs from the Greenland case in the sense of being much more rapid. The I6G target curve for ice volume change highlights the Antarctic contributions to two crucial meltwater pulses (MWPs). MWP1a accounts for an initial 2 m sea level equivalent ice loss between 14.5 and 14 kyr B.P., and is followed by a further loss of about 6 m of ice during MWP1b (between 12 and 10 kyr B.P.). The geographical sources of MWP1a and MWP1b will be discussed below, where results from our nudged simulations will show how the I6G reconstruction for Antarctica discussed in *Argus et al.* [2014] robustly anticipated the ice thickness history for Antarctica that *Golledge et al.* [2014] subsequently obtained through detailed tuning of a coupled ice sheet-ocean model. Before discussing this aspect of the ice dynamics simulations, however, it will prove useful to consider how application of our nudging procedure has affected the quality of fits achieved to the crucial GPS measurements that constituted the primary observational constraints on the I6G reconstruction discussed in *Argus et al.* [2014].

To this end Figure 11 depicts contour plots of modern vertical displacement rate, $\partial B/\partial t(0)$, from a $\tau_f = 20$ years simulation (middle frame) compared to I6G (left frame, with the difference shown in the right frame). *Argus et al.* [2014] fit the I6G reconstruction of regional ice history to GPS observations from 42 sites, and the locations of the sites are indicated by these authors' four-letter codes in the right-hand portion of the figure. The scatterplot in Figure 12 shows the corresponding observations and their error bars together with the predictions of I6G and of the three nudged simulations with $\tau_f = 20$ years, $\tau_f = 100$ years, and $\tau_f = 200$ years. Figures 11 and 12 both demonstrate that the $\tau_f = 20$ year prediction of vertical uplift rate agrees well with the I6G prediction within the limits represented by the observational (2σ) error bars. Increasing the nudging time scale, τ_f, to weaker 100 year and 200 year values preserves good fits on the whole, but the scatterplot and the I6G misfits plotted in Figure 13 indicate regional sensitivities that are most prominent near the Cordiner Peaks (crdi) GPS location. Other localized regions of overpredicted and underpredicted vertical uplift rate are visible

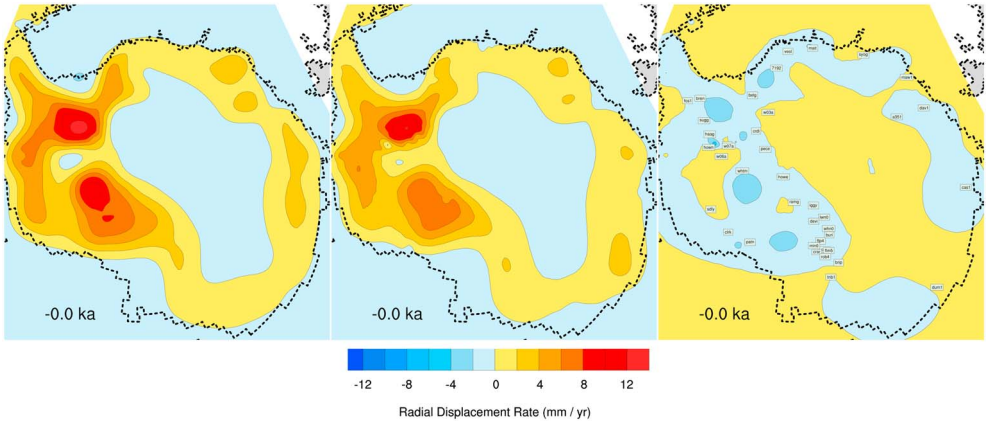

Figure 11. Modern vertical displacement rates (in mm/yr) computed for Antarctica by applying the (left) full GIA-based theory to I6C and (middle) to simulation results with $\tau_f = 20$ years (middle). (right) The difference between the two and the locations of the 42 sites at which *Argus et al.* [2014] compared I6G to GPS observations.

around the margins of the Antarctic ice sheet but fail to register in the scatterplot because their positions fall between GPS sites.

The concentration of GPS misfits at the Antarctic ice sheet margins as τ_f increases prompts return to the point concerning high-order physics in these regions that is being smoothed by shallow-ice dynamics. The observationally consistent smoothing of the I6G solution (left) by ice dynamics at $\tau_f = 20$ years (right) is illustrated in Figure 14, as it applies to the relative surface elevation of the modern Antarctic ice sheet with respect to the LGM time slice. Even though strong nudging to I6G minimizes the impact of dynamical smoothing at this timescale, it is clear that the effects are sufficient to transform the manifestly "blocky" reconstruction into a more realistic pattern of ice loss. "Oversmoothed" solutions diverge from observational consistency as weaker nudging enhances inadequately modeled dynamical effects, which would depend upon higher-order ice physics and better parameterizations for accurate representation.

Setting aside local variations in the quality of fits to modern GPS data, we can follow *Argus et al.* [2014] in computing global error measures based on weighted root mean square (wrms) residuals at the 42 relevant observational sites. Table 1 above shows the wrms errors with respect to I6G and the three nudged simulations, along with the weighted means of the same residuals. Errors and residuals computed for the results of *Whitehouse et al.* [2012] are also reproduced from *Argus et al.* [2014] for comparison. It is clear that even the strongly nudged (and therefore weakly smoothed) simulation with $\tau_f = 20$ years exhibits some degradation from the wrms error of I6G, but the increase from 0.90 m/yr to 1.18 m/yr is not particularly significant. The $\tau_f = 100$ year and $\tau_f = 200$ year simulations show larger wrms errors of 1.74 m/yr and 1.81 m/yr, respectively,

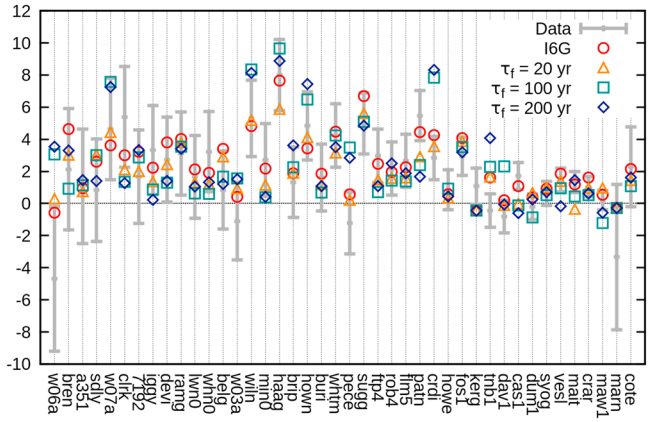

Figure 12. Scatterplot comparing simulated uplift rates from cases with $\tau_f = 20$ years (orange triangles), $\tau_f = 100$ years (cyan squares), and $\tau_f = 200$ years (blue diamonds) with I6G (red circles) and with observations at the 42 stations depicted in Figure 11 (grey error bars spanning data variance).

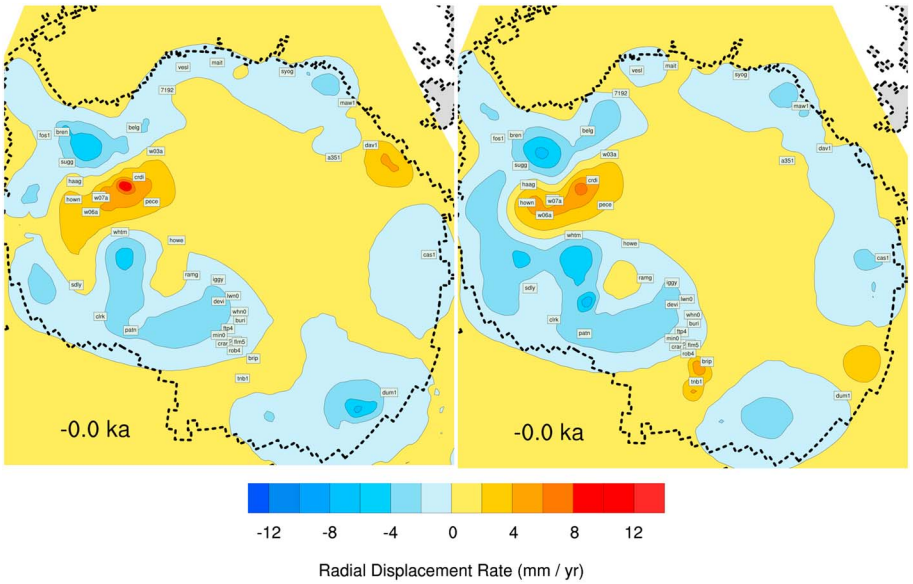

Figure 13. Modern vertical displacement rate misfits analogous to ($\tau_f = 20$ years) Figure 11 (right) for (left) $\tau_f = 100$ years and (right) $\tau_f = 200$ years nudging timescales.

but even these are no worse than the comparable misfits of other published simulation results (the error associated with the predictions of the *Whitehouse et al.* [2012] glaciation history coincidentally happens to be the same as our worst case 1.81 m/yr value). Weighted mean residuals for the nudged simulations are smaller in amplitude, but opposite in sign, in relation to the I6G and *Whitehouse et al.* [2012] results.

Having established that the nudged simulation with $\tau_f = 20$ years smooths out all unnatural blockiness in the I6G solution while preserving its observational consistency, we will conclude this subsection with a fuller discussion of the detailed ice dynamical phenomenology that the model predicts to be occurring at the times of MWP1a and MWP1b. Figure 15 shows contour plots of grounded ice elevation and floating ice shelf thickness from the simulated Antarctic ice sheet at $t = 16$ kyr, 14.5 kyr, 14 kyr, 12 kyr, and 10 kyr B.P. These are critical periods in the deglaciation of Antarctica from LGM to Holocene conditions, and Figure 16 complements Figure 15 by depicting the average rates of grounded ice thickness change over time intervals beginning at

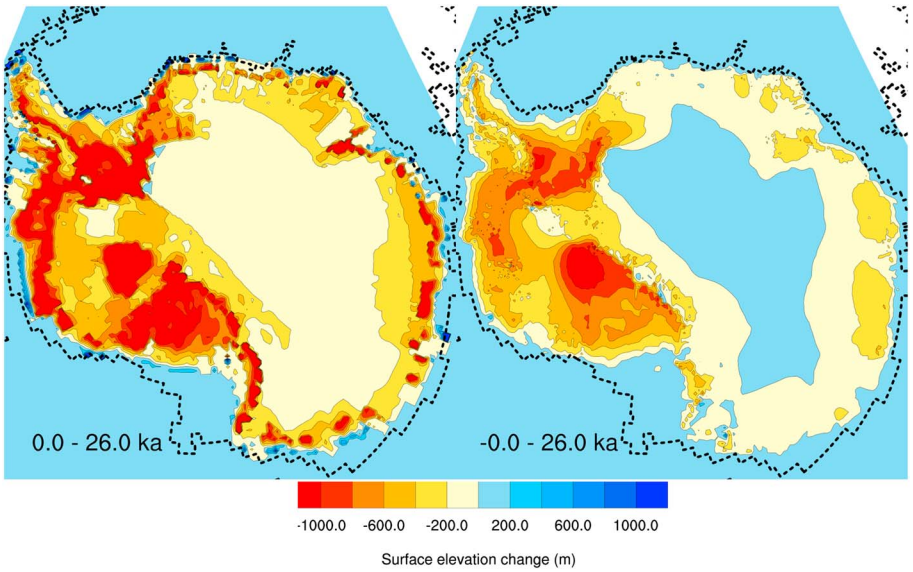

Figure 14. Contour plots illustrating (left) how the I6G reconstruction of LGM-to-modern ice elevation change is smoothed by ice dynamics at nudging timescale (right $\tau_f = 20$ years, from simulation in Figure 15).

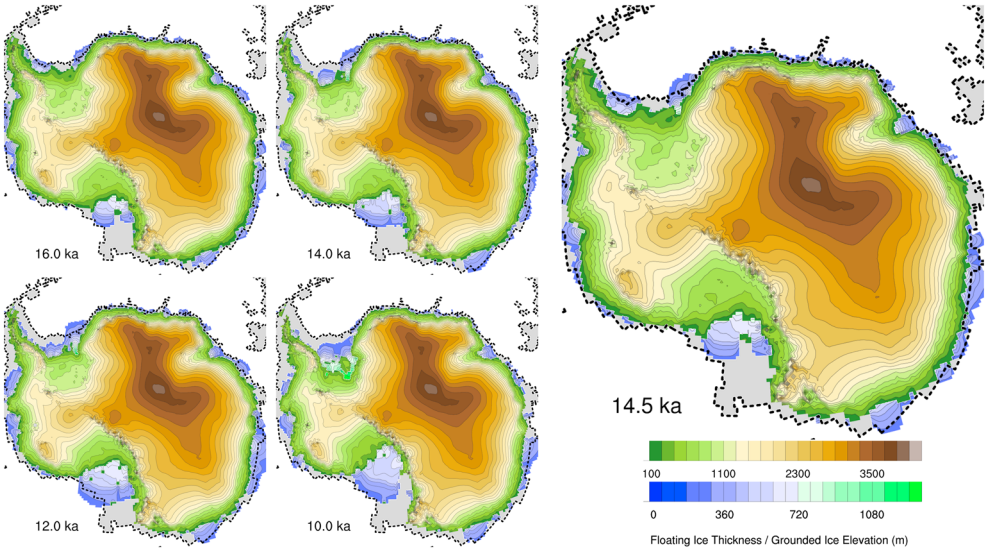

Figure 15. Contour plots of grounded ice elevation and floating ice thickness from the $\tau_f = 20$ year simulation at crucial points in the post-LGM evolution of the Antarctic ice sheet.

the corresponding frames. The contour plots in Figure 16 have been formatted for consistency with the presentation of *Golledge et al.* [2014], wherein the authors discuss dynamical simulations of Antarctic ice shelves that thermodynamically interact with the state of a simple coupled ocean model. The large right-hand panel in the figure highlights the average mass loss rate over the 500 year duration of MWP1a, while the corresponding frame in Figure 15 highlights the ice distribution at the onset of this event. The bottom left-hand panels of the two figures present the same information for the longer duration of MWP1b (between 12 kyr and 10 kyr B.P.), while the other three panels fill out the picture by showing the initial ice distribution and mass loss rate for other time intervals.

Even though we have made no attempt to follow *Golledge et al.* [2014] in dynamically modeling the complex effects of ocean climate on the base of the ice shelves, our results agree remarkably well with this work solely on account of the ice history tuning that *Argus et al.* [2014] and *Peltier et al.* [2015] previously applied to make I6G consistent with GPS, RSL, and exposure age dating observations. Our Figure 16 very similarly identifies the source of the Antarctic contribution to MWP1a with a region at the base of the Antarctic Peninsula, where a large ice margin retreat took place over the relevant time period. Referring back to Figure 10, the approximately 2 m portion of MWP1a that I6G associates with Antarctica is in good agreement with the 1.7–4.3 m range obtained by *Golledge et al.* [2014], who report a total MWP1a amplitude of at least 14 m consistently with the 15–20 m I6G total. These results support the hypothesis that MWP1a came primarily from the now-extinct Northern Hemisphere ice sheets [*Peltier*, 2005] and contradict alternative explanations in which the relevant ice mass loss was imagined to have been dominated by the Antarctic contribution [*Clark et al.*, 2002]. I6G, the results of *Golledge et al.* [2014], and the results of our new nudged simulations all suggest that the major Antarctic-dominated contribution to global deglaciation (i.e., the 6 m contribution to MWP1b) occurred only after approximately 2000 years of relative stability subsequent to the end of MWP1a. Some controversy has arisen on account of the fact that more elaborate assumptions involving weak or nonexistent MWP1b events

Table 1. Error Measures

Error Measure (Right) Model (Down)	Weighted RMS Error (mm/yr)	Weighted Mean Residual (mm/yr)
ICE 6G (VM5a)	0.90	−0.30
$\tau_f = 20$ years	1.18	0.13
$\tau_f = 100$ years	1.74	0.22
$\tau_f = 200$ years	1.81	0.08
Whitehouse et al. [2012]	1.81	−0.56

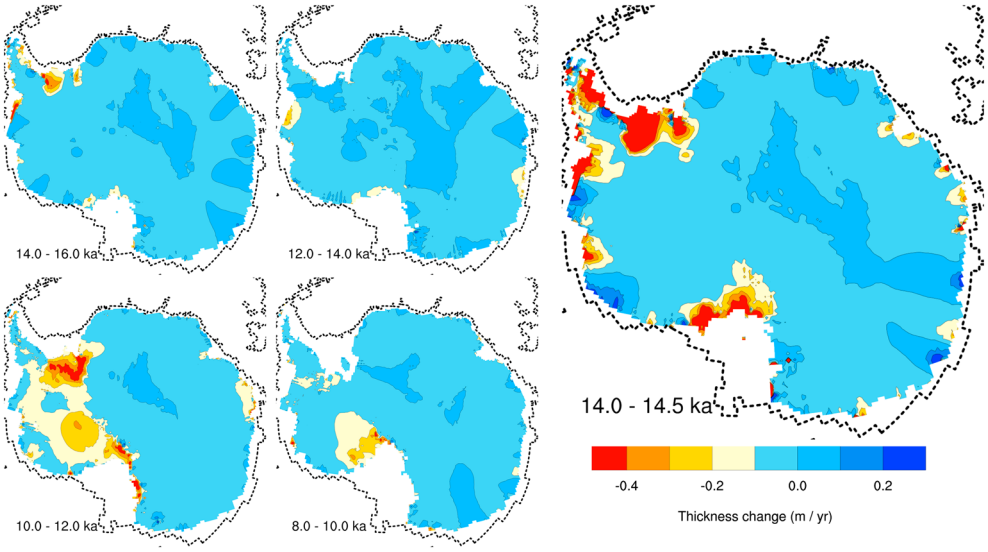

Figure 16. Contour plots of average rate of grounded ice thickness change over the intervals bounded by the frames in Figure 15.

may explain quantitative measurements of the kind discussed in this paper, but sedimentary records from the Antarctic shelf provide additional, qualitative evidence suggesting the existence of a focused contribution to eustatic sea level rise from Antarctica at MWP1b time (the most recent discussions on this topic appear in *Argus et al.* [2014] and *Peltier et al.* [2015]). Even if future analyses based upon more rigorous physical and observational constraints were to invalidate the I6G estimate of the magnitude of MWP1b, they would have to explain how a less dramatic event produced the sedimentary record rather than discounting the existence of MWP1b entirely.

Unlike the analyses of *Golledge et al.* [2014], our simulations aim to demonstrate the glaciological consistency of the I6G glaciation history reconstruction in a generic ice-dynamical sense rather than being tuned to demonstrate the plausibility of some particular explanation for the Antarctic deglaciation sequence. Figure 15 clarifies the reconfiguration of grounded and floating ice corresponding to the mass losses of Figure 16, which may or may not be explicable in terms of the particular hypothesis proposed by *Golledge et al.* [2014]. It is nevertheless interesting that the two methodologies have led to the same conclusion concerning both the magnitude of the contribution of Antarctica to Meltwater Pulse 1A and to its geographical origins.

5. Conclusions

By nudging local simulations of the glaciation histories of Greenland and Antarctica to those of the GIA-inferred I6G model over the timescale of the most recent glaciation-deglaciation cycle, we have provided a means whereby this methodology may be employed to investigate the glaciological consistency of the GIA-inferred models of these histories. The mass balance nudging methodology we have developed also provides an alternative means of assessing the nonuniqueness of the glaciation histories delivered by application of the GIA-based reconstruction technique. Based upon the fact that we can keep nudged dynamical simulations consistent with I6G without giving rise to gross physical anomalies, we can conclude that the GIA methodology not only successfully passes the critical test of glaciological consistency but is also delivering additional important insights into ice physical processes. Concerning the description of ice dynamics at grounding lines and at the edges of ice sheets in general, the fact that consistency cannot be maintained with nudging at or below the amplitude of surface mass balances ($\tau_f \approx$ 1000+ years) points to the inadequacy of established parameterizations of the higher-order physics that must have played a crucial role during catastrophic events such as MWP1a and MWP1b. A great deal of research effort has already been targeted toward the improvement of models of ice sheet dynamical behavior, but the logical interpretation of our methods provides a coherent basis for evaluating such efforts with respect to the extensively validated I6G reconstruction. Greatly improved ice models and new observations will undoubtedly reveal the need for the further

revision of I6G, but we have shown that there is no reason to suppose that the leading-order "coarse-grained" validity of this reconstruction is in any way inconsistent with rational ice dynamics.

Concerning the new results that our nudging methodology has delivered concerning the glaciation history of the Greenland ice sheet, the primary contribution of the work reported herein has concerned the post LGM mass loss from this system. In TP02 and *Tarasov and Peltier* [2004], it was suggested that the best estimate of this contribution to the post LGM rise of sea level was approximately 2 m. Here we have suggested that the data constraining this mass loss would be equally accepting of a 50% increase in this estimate, primarily derivative of the application of an improved calving parameterization.

Insofar as our new analysis of Antarctic glaciation history is concerned, this has proved a much more severe test of the nudging methodology, especially regarding the geographical origins and magnitudes of the Antarctic contributions to meltwater pulses 1A and 1B. In *Argus et al.* [2014] it was demonstrated that application of the GIA reconstruction methodology predicted that if there was a contribution from Antarctica to meltwater pulse 1A, this was predicted to be of no more than 2 m in the associated net eustatic sea level rise. It was furthermore, although not exclusively, predicted to have emanated from the geographical region near the base of the Antarctic Peninsula. These same characteristics were immediately thereafter independently suggested by *Golledge et al.* [2014] on the basis of an entirely different line of argument. That such a modest contribution to MWP 1A could have come from Antarctica is in accord with the arguments in *Peltier* [2005] to the effect that the majority of this pulse must have come from Northern Hemisphere sources.

Appendix A: PISM Mass Balance, Ice Flux, and Thermodynamics

A1. Mass Balance

In typical paleoclimate ice modeling applications, typical ice models like PISM parameterize surface mass balance, $G_s(\Omega, t)$, through a positive degree day (PDD) scheme along the following lines; i.e.,

$$G_s(\Omega,t) = \frac{12}{t_Y} \times \begin{cases} S(\Omega,t) - \gamma_{\text{snow}}\Pi(\Omega,t) & \text{for } S(\Omega,t) > \gamma_{\text{snow}}\Pi(\Omega,t) \\ -\gamma_{\text{ice}}\left[\Pi(\Omega,t) - \frac{S(\Omega,t)}{\gamma_{\text{snow}}}\right] & \text{otherwise,} \end{cases} \tag{A1}$$

in which $S(\Omega, t)$ is the total local snowfall in millimetres over the course of a month (i.e., over time $t_Y/12$, where t_Y is the length of a year), and $\Pi(\Omega, t)$ is the local number of PDDs for that month. Energy associated with PDDs is deemed to go first into melting snow at a rate of γ_{snow} mm/PDD; surplus snowfall turns to ice, while surplus PDDs go into melting ice at a rate of γ_{ice} mm/PDD. S and Π are determined by the following statistical model; i.e.,

$$\begin{aligned} S(\Omega,t) &= \int_{t_i(t)}^{t_f(t)} \Psi\left(-\sigma_{\text{NS}}, 0, \Omega, t'\right) P_{\text{surf}}\left(\Omega, t'\right) \mathrm{d}t' \\ \Pi(\Omega,t) &= \frac{12 t_D \sigma_{\text{PDD}}}{t_Y} \int_{t_i(t)}^{t_f(t)} \Psi\left(\sigma_{\text{PDD}}, 1, \Omega, t'\right) \mathrm{d}t' \\ \Psi(\sigma,\alpha,\Omega,t) &\equiv \frac{1}{\sigma\sqrt{2\pi}} \int_0^\infty \left[1 + \alpha\left(\frac{T}{\sigma} - 1\right)\right] \times \exp\left[\frac{-\left(T - T_{\text{surf}}(\Omega,t)\right)^2}{2\sigma^2}\right] \mathrm{d}T, \end{aligned} \tag{A2}$$

in which $T_{\text{surf}}(\Omega, t)$, and $P_{\text{surf}}(\Omega, t)$ are climatological surface temperature and precipitation fields, σ_{PDD} and σ_{NS} are the respective variances of temperature on days with nonfreezing conditions and on days with precipitation, t_D is the length of a day, and

$$t_i(t) \equiv \left\lfloor \frac{12t}{t_Y} \right\rfloor \frac{t_Y}{12} \quad \text{and} \quad t_f(t) \equiv t_i\left(t + \frac{t_Y}{12}\right) \tag{A3}$$

are the start and end of the current month (at time t). The climatological surface temperature and precipitation fields are treated as offsets from a modern annual climate, i.e.,

$$\begin{aligned} T_{\text{surf}}(\Omega,t) &= T_{\text{surf}}\left(\Omega, -t_Y + t - 12t_i\left(t/12\right)\right) + \Delta T(\Omega,t) \\ P_{\text{surf}}(\Omega,t) &= P_{\text{surf}}\left(\Omega, -t_Y + t - 12t_i\left(t/12\right)\right) \times \exp\left[\eta \Delta T(\Omega,t)\right], \end{aligned} \tag{A4}$$

in which the exponential coefficient, η, models precipitation deviation in terms of temperature deviation, $\Delta T(\Omega, t)$ (equation (16)).

Newer ice models like PISM have introduced some parameterizations that couple the basal mass balance, G_b, to the budget of meltwater beneath grounded ice (see section A1 below), but ad hoc representations of G_b for floating ice shelves are still very specific to particular studies [e.g., *Pollard and DeConto*, 2009; *Joughin et al.*, 2014].

A2. Ice Flux

In discussing the problem that determines the local 3-D velocity, $\mathbf{u}(\Omega, z, t)$, of ice, we will project horizontal coordinates onto a local stereographic plane and use the following notation, i.e.,

$$\begin{aligned}\mathbf{u}(\mathbf{x}, t) &\equiv \begin{bmatrix} u \\ v \\ w \end{bmatrix}(x, y, z, t) = \begin{bmatrix} u_1 \\ u_2 \\ u_3 \end{bmatrix}\left(x_1, x_2, x_3, t\right) \\ &= u\hat{\mathbf{x}} + v\hat{\mathbf{y}} + w\hat{\mathbf{z}} = u_1\hat{\mathbf{x}}_1 + u_2\hat{\mathbf{x}}_2 + u_3\hat{\mathbf{x}}_3,\end{aligned} \tag{A5}$$

while also introducing the notation

$$\overline{\Phi}(x, y, t) = \frac{1}{l}\int_{B_i}^{H} \Phi(x, y, z, t)\, dz.$$

to refer to the vertical average of a field, $\Phi(x, y, z, t)$, over the ice column. $\mathbf{u}$ is approximated as a sum of two velocity fields determined by the following equations, i.e.,

$$\begin{aligned}\mathbf{u} &\approx \mathbf{u}^{3D} + \mathbf{u}^{2D} \\ \mathbf{u}^{3D} &= -\rho_i g(1 - C)\int_B^H \nu^{-1}(H - z)\nabla_h H dz \\ \sum_{j=1}^{2}\left\{\frac{\partial}{\partial x_j}\left(l\overline{\sigma}_i \cdot \hat{\mathbf{x}}_j\right) + \frac{\partial}{\partial x_i}\left(l\left(\overline{\sigma}_j \cdot \hat{\mathbf{x}}_j\right)\right)\right\} &= \rho_i g l\frac{\partial H}{\partial x_i} - \alpha^2 u_i^{2D} \\ \overline{\sigma}_i \cdot \hat{\mathbf{x}}_j &\approx \overline{\nu}\left(\frac{\partial u_i^{2D}}{\partial x_i} + \frac{\partial u_j^{2D}}{\partial x_i}\right)\end{aligned} \tag{A6}$$

in which $\mathbf{u}^{3D}$ is the "shallow-ice approximation" (SIA) of the shearing flow of thin, grounded ice [e.g., *Hutter*, 1983], while $\mathbf{u}^{2D}$ is the shelfy-stream approximation (SSA) of stretching flow that may exist in ice shelves and in regions of strong basal sliding [*MacAyeal*, 1989]. Both of these flow regimes are approximations of the Full Stokes (FS) model [e.g., *Pattyn et al.*, 2008] that more generally determines $\mathbf{u}$ along with the scalar pressure field, $p(x, y, z, t)$, through the following four coupled divergence equations, i.e.,

$$\begin{aligned}\nabla \cdot \mathbf{u} = 0 \quad \nabla \cdot \boldsymbol{\sigma}_i &= \frac{\partial}{\partial x_i}\left(p + \rho g x_3\right) \\ \boldsymbol{\sigma}_i \equiv \nu\boldsymbol{\varepsilon}_i \qquad \boldsymbol{\varepsilon}_i &\equiv \nabla u_i + \frac{\partial \mathbf{u}}{\partial x_i},\end{aligned} \tag{A7}$$

in which g is accelleration due to gravity, $\boldsymbol{\varepsilon}_i$ and $\boldsymbol{\sigma}_i$ are the respective ith rows of the strain rate and deviatoric stress tensors (for $i = 1$, 2, or 3), and ν is the viscosity of ice. Viscosity depends nonlinearly upon both $\mathbf{u}$ and p, and upon ice thermodynamics that also couple to the flow structure through the basal friction (α^2 in the elliptic equation pair determining $\mathbf{u}^{2D}$ in equation (A6)). This coupling will be discussed in the following subsection, and the remainder of the current subsection will deal with the horizontal BCs of the elliptic equation for $\mathbf{u}^{2D}$.

Albrecht et al. [2011] described a semiheuristic numerical calving parameterization by which the PISM model approximates the horizontal kinematic BC of equations ((18), (19)), with $\mathbf{U}_c$ given by the following eigen-calving rule; i.e.,

$$\begin{aligned}\mathbf{U}_c &= \begin{cases} \frac{\mathbf{u}^{2D}}{\|\mathbf{u}^{2D}\|}U_c & \text{if } U_c < 0 \\ 0 & \text{if } U_c \le 0 \end{cases} \\ U_c &\equiv K\left[\frac{\partial}{\partial x}\left(\mathbf{u}^{2D}\cdot\mathbf{x}\right)\frac{\partial}{\partial y}\left(\mathbf{u}^{2D}\cdot\mathbf{y}\right) - \frac{\partial}{\partial y}\left(\mathbf{u}^{2D}\cdot\mathbf{x}\right)\frac{\partial}{\partial x}\left(\mathbf{u}^{2D}\cdot\mathbf{y}\right)\right],\end{aligned} \tag{A8}$$

in which the constant K multiplies the determinant of the vertically averaged horizontal strain rate tensor. Since two equations are involved, an additional horizontal BC is required and formulated along the following lines; i.e.,

$$\overline{\sigma}_i \cdot \nabla_h C_l = \left(\frac{1}{2}\rho_i g l^2 - \overline{p_{\mathrm{ocn}}}\right) \hat{\mathbf{x}}_i \cdot \nabla_h C_l \quad \text{for} \quad i = 1, 2, \tag{A9}$$

in which

$$\overline{p_{\mathrm{ocn}}} = \frac{1}{2}\rho_w g \min\left\{B_i^2, 0\right\}$$

is the vertically averaged ocean pressure on the ice edge.

A3. Thermodynamics and Basal Processes

Introducing the notation

$$\begin{aligned} \Phi_K(x,y,t) &\equiv \Phi\left(x,y,\xi_K(x,y,t),t\right) \\ \mathbf{n}_K^* &\equiv \nabla\left[z - \xi_K(x,y,t)\right] \qquad \left(\xi_s,\xi_b\right) \equiv \left(H,B_i\right)(x,y,t) \\ \mathbf{n}_K &\equiv \left(\mathbf{n}_K^* \cdot \mathbf{n}_K^*\right)^{-1/2} \mathbf{n}_K^* \qquad\qquad \mathcal{T}_K\mathbf{A} \equiv \mathbf{A} - \mathbf{n}_K\left(\mathbf{n}_K \cdot \mathbf{A}\right) \end{aligned} \tag{A10}$$

to refer to the respective surface and basal values of a field $\Phi(x,y,z,t)$ (Φ_s and Φ_b), of the normal vectors ($\mathbf{n}_s$ and $\mathbf{n}_b$), and of the tangential projection matrices ($\mathcal{T}_s$ and $\mathcal{T}_b$), we can write down the following temperature-based formulation for the polythermal (i.e., "cold") ice energy equation and its BCs; i.e.,

$$\begin{aligned} \frac{\partial}{\partial t}\left[\rho c_i(T)T\right] + \nabla \cdot \left[\rho c_i(T)T\mathbf{u} - \kappa\nabla T\right] &= 4\nu\epsilon^2 \\ T_s &= T_{\mathrm{surf}} \\ \kappa\mathbf{n}_b \cdot \nabla T_b - \alpha^2 \mathbf{u}_b \cdot \mathbf{u}_b &= -\kappa_{\mathrm{bed}}\mathbf{n}_b \cdot \nabla T_{\mathrm{bed}}, \end{aligned} \tag{A11}$$

in which the newly introduced quantities are the thermal diffusivities of ice and bedrock (κ and κ_{bed}, respectively), the bedrock temperature distribution, T_{bed}, the principal strain rate,

$$\epsilon \equiv \sqrt{\sum_{i=1}^{3} \boldsymbol{\epsilon}_i \cdot \boldsymbol{\epsilon}_i}, \tag{A12}$$

and the temperature-dependent specific heat, $c_i(T)$, of polythermal ice that is below its pressure adjusted melting point, $T_m(p)$ (which is always about $T_m(0) \approx 0°\mathrm{C}$ at the surface). The bed temperature has most often been obtained by simultaneously solving a simplified vertical diffusion equation,

$$\begin{aligned} \frac{\partial T_{\mathrm{bed}}}{\partial t} &= \kappa_r \frac{\partial^2 T_{\mathrm{bed}}}{\partial z^2} \\ T_{\mathrm{bed}}(x,y,B) &= T_b(x,y,t) \\ -\kappa_r \frac{\partial T_{\mathrm{bed}}}{\partial z}(x,y,B - 5\mathrm{km}) &= Q_{\mathrm{geo}}(x,y). \end{aligned} \tag{A13}$$

in a thermal buffer zone (say, a 5 km thickness of lithosphere below the grounded ice) that is heated from below by the geothermal heat flux, Q_{geo}.

In contrast to older, purely polythermal ice models like the versions of the UofT GSM used in *Tarasov and Peltier* [2002] (hereafter TP02) and associated works, PISM can also represent temperate ice regions in which ice coexists with a liquid water fraction, ω, at its pressure adjusted melting point, $T_m(p)$. A thermal-hydraulic buffer model at the lower boundary can in this context explicitly simulate a water layer of thickness W as follows:

$$\frac{\partial W}{\partial t} = D_w \nabla^2 W + d_w \int_B^H \omega(E,p)\mathrm{d}z, \tag{A14}$$

in which D_w and d_w are, respectively, the diffusivity and drainage rate of ice with water fraction, $\omega(E,p)$, that depends upon pressure, p, and enthalpy, E. For latent heat of melting Λ and arbitrary reference temperature T_0, enthalpy can be determined in terms of temperature, water fraction, and pressure as follows; i.e.,

$$E(T,\omega,p) = \begin{cases} E_i(T) & T < T_m(p) \\ E_i(T_m(p)) + \omega\Lambda & T = T_m(p) \end{cases}$$

$$E_i(T) = \int_{T_0}^{T} c_i(T')\mathrm{d}T', \tag{A15}$$

while temperature and water fraction can be determined in terms of enthalpy and pressure by the following inverse relations, i.e.

$$(T,\omega)(E,p) = \begin{cases} (T_i(E),0) & E < E_i(T_m(p)) \\ \left(T_m(p), \frac{E-E_i(T_m(p))}{\Lambda}\right) & \text{otherwise} \end{cases}$$

$$\frac{\partial T_i(E)}{\partial E} = [c_i(T_i)]^{-1} \quad \text{with} \quad T_i(0)=T_0 \tag{A16}$$

[see *Aschwanden et al.*, 2012]. The use of an enthalpy-pressure formulation that accommodates temperate ice naturally requires a suitable replacement for the polythermal ice energy equation (A12). We will not discuss this aspect of the literature because the associated mathematics is complex and would only be distracting in the present context.

Given an enthalphy-based formulation of the energy equation and an associated basal hydrology model, the parameterizations of basal friction, α^2, and plastic ice viscosity, ν, are represented along the following lines; i.e.,

$$\alpha^2 = \tau_c \frac{\left|\mathcal{T}_b \mathbf{u_b}\right|^{q-1}}{U_{\mathrm{ref}}^q}, \quad \text{and} \quad \nu = \frac{1}{2}\epsilon(\epsilon A)^{-\frac{1}{n}} \tag{A17}$$

in which U_{ref} is a reference velocity, and in which q and n are phenomenological power law exponents (the Glen exponent, in the case of n). The till strength, τ_c, and the ice hardness, A, are prescribed, respectively, by a Mohr-Coulomb law and an Arrhenius relation, i.e.,

$$\tau_c(W,I,B) = c_0 + \rho g I \tan\phi(B) \times \begin{cases} 1 - f_w \frac{W}{W_0} & \text{for } W < W_0 \\ 1 - f_w & \text{otherwise,} \end{cases}$$

$$A(E,p) = A_0(E,p)\exp\left(\frac{-Q(E,p)}{RT(E,p)}\right), \tag{A18}$$

which parameterize how the till is strengthened by overlying ice and weakened by underlying water, and how phenomenological ice hardness, $A_0(E,p)$, is reduced close to the melting point described by a thermodynamic activation energy, $Q(E,p)$, and by the universal gas constant, R. The constants c_0, f_w, and W_0 specify a base till strength, a maximum water fraction, and a reference water column height (with typical values 0, 0.95, and 2 m, respectively), and the till fraction angle, $\phi(B)$, modifies the Mohr-Coulomb law based on bottom topography through the following parameterization; i.e.,

$$\phi(B) = \begin{cases} \phi_{\min} & \text{for } B < B_{\min} \\ \phi_{\min} + \left(\frac{B-B_{\min}}{B_{\max}-B_{\min}}\right)(\phi_{\max}-\phi_{\min}) & \text{for } B_{\min} \le B \le B_{\max} \\ \phi_{\max} & \text{for } B_{\max} < B, \end{cases} \tag{A19}$$

in which the constants $\phi_{\min}$, $\phi_{\max}$, $B_{\min}$, and $B_{\max}$ straightforwardly prescribe a linear transition between constant threshold values.

Acknowledgments
Partial support for this study has been provided by the Nuclear Waste Management Organization (NWMO). The research of W.R.P. at Toronto is supported by NSERC Discovery grant A9627. All of the computational analyses reported in this paper were performed on the SciNet High Performance Computing facility which is a component of the Compute Canada HPC platform. The data underlying the reported analyses are cited in conformity with the AGU Data Policy: I6G-related data sets are available as supplemental materials to *Peltier et al.* [2015] and on WRP's web site (http://www.atmosp.physics.utoronto.ca/~peltier/data.php); the source codes for version 0.6 of the PISM ice sheet model were obtained through the model developers' public web site (http://pism-docs.org/wiki/doku.php?id=stable_version) along with the supporting information needed to reproduce SeaRISE analyses of Greenland and Antarctica from the cited, publicly available climatological and geophysical data sets.

References

Albrecht, T., M. Martin, M. Haseloff, R. Winkelmann, and A. Levermann (2011), Parameterization for subgrid-scale motion of ice-shelf calving fronts, *Cryosphere*, *5*(1), 35–44.

Argus, D. F., W. R. Peltier, R. Drummond, and S. Moore (2014), The Antarctic component of glacial isostatic adjustment model ICE-6G_C (VM5a) based upon GPS measurements of vertical motion of the crust, exposure age dating of ice thickness variations and relative sea level histories, *Geophys J. Int.*, *198*(1), 537–563, doi:10.1093/gji/ggu140.

Aschwanden, A., E. Bueler, C. Khroulev, and H. Blatter (2012), An enthalpy formulation for glaciers and ice sheets, *J. Glaciol.*, *58*(209), 441–457.

Bamber, J. L., R. L. Layberry, and S. Gogineni (2001), A new ice thickness and bed data set for the Greenland ice sheet: 1. Measurement, data reduction, and errors, *J. Geophys. Res.*, *106*(D24), 33,773–33,780.

Bindschadler, R. A., et al. (2013), Ice-sheet model sensitivities to environmental forcing and their use in projecting future sea level (the SeaRISE project), *J. Glaciol.*, *59*(214), 195–224.

Blatter, H. (1995), Velocity and stress fields in grounded glaciers: A simple algorithm for including deviatoric stress gradients, *J. Glaciol.*, *41*(138), 333–344.

Bueler, E., J. Brown, and C. Lingle (2007), Exact solutions to the thermomechanically coupled shallow-ice approximation: Effective tools for verification, *J. Glaciol.*, *53*(182), 499–516.

Clark, J. A., W. E. Farrell, and W. R. Peltier (1978), Global changes in postglacial sea level: A numerical calculation, *Quat. Res.*, *9*(3), 265–287.

Clark, P. U., J. Mitrovica, G. Milne, and M. Tamisiea (2002), Sea-level fingerprinting as a direct test for the source of global meltwater pulse IA, *Science*, *295*(5564), 2438–2441.

Ettema, J., M. R. van den Broeke, E. van Meijgaard, W. J. van de Berg, J. L. Bamber, J. E. Box, and R. C. Bales (2009), Higher surface mass balance of the Greenland ice sheet revealed by high-resolution climate modeling, *Geophys. Res. Lett.*, *36*, L12501, doi:10.1029/2009GL038110.

Farrell, W., and J. A. Clark (1976), On postglacial sea level, *Geophys. J. Int.*, *46*(3), 647–667.

Golledge, N. R., L. Menviel, L. Carter, C. J. Fogwill, M. H. England, G. Cortese, and R. H. Levy (2014), Antarctic contribution to meltwater pulse 1a from reduced Southern Ocean overturning, *Nat. Commun.*, *5*, 5107, doi:10.1038/ncomms6107.

Gomez, N., D. Pollard, J. X. Mitrovica, P. Huybers, and P. U. Clark (2012), Evolution of a coupled marine ice sheet-sea level model, *J. Geophys. Res.*, *117*, F01013, doi:10.1029/2011JF002128.

Hutter, K. (1983), *Theoretical Glaciology: Material Science of Ice and the Mechanics of Glaciers and Ice Sheets*, vol. 1, Springer, Dordrecht, Netherlands.

Imbrie, J., and A. McIntyre (2006), *SPECMAP Time scale developed by Imbrie et al., 1984 based on normalized planktonic records (Normalized O-18 vs. Time, Specmap. 017)*, PANGAEA–Data Publisher for Earth and Environmental Science, doi:10.1594/PANGAEA.441706.

Johnsen, S. J., et al. (1997), The δ18O record along the Greenland Ice Core Project deep ice core and the problem of possible Eemian climatic instability, *J. Geophys. Res.*, *102*(C12), 26,397–26,410.

Joughin, I., B. E. Smith, and B. Medley (2014), Marine ice sheet collapse potentially under way for the Thwaites Glacier basin, West Antarctica, *Science*, *344*(6185), 735–738.

Larour, E., H. Seroussi, M. Morlighem, and E. Rignot (2012), Continental scale, high order, high spatial resolution, ice sheet modeling using the Ice Sheet System Model (ISSM), *J. Geophys. Res.*, *117*, F01022, doi:10.1029/2011JF002140.

Le Brocq, A., A. J. Payne, and A. Vieli (2010), An improved Antarctic dataset for high resolution numerical ice sheet models (ALBMAP v1), *Earth Syst. Sci. Data*, *2*, 247–260.

MacAyeal, D. R. (1989), Large-scale ice flow over a viscous basal sediment: Theory and application to ice stream B, Antarctica, *J. Geophys. Res.*, *94*(B4), 4071–4087.

Marshall, S. J., L. Tarasov, G. K. Clarke, and W. R. Peltier (2000), Glaciological reconstruction of the Laurentide Ice Sheet: Physical processes and modelling challenges, *Can. J. Earth Sci.*, *37*(5), 769–793.

Nowicki, S., et al. (2013a), Insights into spatial sensitivities of ice mass response to environmental change from the SeaRISE ice sheet modeling project I: Antarctica, *J. Geophys. Res. Earth Surf.*, *118*, 1002–1024, doi:10.1002/jgrf.20081.

Nowicki, S., et al. (2013b), Insights into spatial sensitivities of ice mass response to environmental change from the SeaRISE ice sheet modeling project II: Greenland, *J. Geophys. Res. Earth Surf.*, *118*, 1025–1044, doi:10.1002/jgrf.20076.

Pattyn, F. (2003), A new three-dimensional higher-order thermomechanical ice sheet model: Basic sensitivity, ice stream development, and ice flow across subglacial lakes, *J. Geophys. Res.*, *108*(B8), 2382, doi:10.1029/2002JB002329.

Pattyn, F., et al. (2008), Benchmark experiments for higher-order and Full Stokes ice sheet models (ISMIP-HOM), *Cryosphere Discuss.*, *2*(1), 111–151.

Peltier, W. (1974), The impulse response of a Maxwell Earth, *Rev. Geophys.*, *12*(4), 649–669.

Peltier, W. (1976a), Glacial-isostatic adjustment—II. The inverse problem, *Geophys. J. R. Astron. Soc.*, *46*(3), 669–705.

Peltier, W. (1976b), Glacio-isostatic adjustment—III. The inverse problem, *Geophys. J.*, *46*, 669–706.

Peltier, W. (1996), Mantle viscosity and ice-age ice sheet topography, *Science*, *273*(5280), 1359–1364.

Peltier, W. (1998), Postglacial variations in the level of the sea: Implications for climate dynamics and solid-Earth geophysics, *Rev. Geophys.*, *36*(4), 603–689.

Peltier, W. (2004), Global glacial isostasy and the surface of the ice-age Earth: The ICE-5G (VM2) model and GRACE, *Annu. Rev. Earth Planet. Sci.*, *32*, 111–149.

Peltier, W. (2005), On the hemispheric origins of meltwater pulse 1a, *Quat. Sci. Rev.*, *24*(14), 1655–1671.

Peltier, W. (2007), *History of Earth Rotation*, vol. 9, pp. 243–293, Elsevier, Oxford, U. K.

Peltier, W., and J. Andrews (1976), Glacial-isostatic adjustment—I. The forward problem, *Geophys. J. R. Astron. Soc.*, *46*(3), 605–646.

Peltier, W., and R. G. Fairbanks (2006), Global glacial ice volume and Last Glacial Maximum duration from an extended Barbados sea level record, *Quat. Sci. Rev.*, *25*(23), 3322–3337.

Peltier, W., and S. B. Luthcke (2009), On the origins of Earth rotation anomalies: New insights on the basis of both "paleogeodetic" data and Gravity Recovery and Climate Experiment (GRACE) data, *J. Geophys. Res.*, *114*, B11405, doi:10.1029/2009JB006352.

Peltier, W., W. Farrell, and J. Clark (1978), Glacial isostasy and relative sea level: A global finite element model, *Tectonophysics*, *50*(2), 81–110.

Peltier, W., R. Drummond, and K. Roy (2012), Comment on "Ocean mass from GRACE and glacial isostatic adjustment" by D. P. Chambers et al., *J. Geophys. Res.*, *117*, B11403, doi:10.1029/2011JB008967.

Peltier, W. R. (1994), Ice age paleotopography, *Science*, *265*(5169), 195–201.

Peltier, W. R., D. F. Argus, and R. Drummond (2015), Space geodesy constrains ice age terminal deglaciation: The global ICE-6G_C (VM5a) model, *J. Geophys. Res. Solid Earth*, *120*, 450–487, doi:10.1002/2014JB011176.

Petit, J., et al. (2001), *Vostok Ice Core Data for 420,000 Years, IGBP PAGES/World Data Center for Paleoclimatology Data Contribution Series# 2001-076*, NOAA/NGDC Paleoclimatology Program, Boulder, Colo.

Pollard, D., and R. M. DeConto (2009), Modelling West Antarctic ice sheet growth and collapse through the past five million years, *Nature*, *458*(7236), 329–332.
Ritz, C., A. Fabre, and A. Letréguilly (1996), Sensitivity of a Greenland ice sheet model to ice flow and ablation parameters: Consequences for the evolution through the last climatic cycle, *Clim. Dyn.*, *13*(1), 11–23.
Rovere, A., M. Raymo, J. Mitrovica, P. Hearty, M. O'Leary, and J. Inglis (2014), The mid-Pliocene sea-level conundrum: Glacial isostasy, eustasy and dynamic topography, *Earth Planet. Sci. Lett.*, *387*, 27–33.
Salameh, T., P. Drobinski, and T. Dubos (2010), The effect of indiscriminate nudging time on large and small scales in regional climate modelling: Application to the mediterranean basin, *Q. J. R. Meteorol. Soc.*, *136*(646), 170–182.
Schoof, C. (2007a), Ice sheet grounding line dynamics: Steady states, stability, and hysteresis, *J. Geophys. Res.*, *112*, F03S28, doi:10.1029/2006JF000664.
Schoof, C. (2007b), Marine ice-sheet dynamics. Part 1. The case of rapid sliding, *J. Fluid Mech.*, *573*, 27–55.
Shapiro, N. M., and M. H. Ritzwoller (2004), Inferring surface heat flux distributions guided by a global seismic model: Particular application to Antarctica, *Earth Planet. Sci. Lett.*, *223*(1), 213–224.
Tarasov, L., and W. Peltier (1997), Terminating the 100 kyr ice age cycle, *J. Geophys. Res.*, *102*(D18), 21,665–21,693.
Tarasov, L., and W. Peltier (1999), Impact of thermomechanical ice sheet coupling on a model of the 100 kyr ice age cycle, *J. Geophys. Res.*, *104*, 9517–9545.
Tarasov, L., and W. Peltier (2000), Laurentide ice sheet aspect ratio in models based on Glen's flow law, *Ann. Glaciol.*, *30*(1), 177–186.
Tarasov, L., and W. Peltier (2002), Greenland glacial history and local geodynamic consequences, *Geophys. J. Int.*, *150*, 198–229.
Tarasov, L., and W. Peltier (2003), Greenland glacial history, borehole constraints, and Eemian extent, *J. Geophys. Res*, *108*(B3), 2143, doi:10.1029/2001JB001731.
Tarasov, L., and W. Peltier (2004), A geophysically constrained large ensemble analysis of the deglacial history of the North American ice-sheet complex, *Quat. Sci. Rev.*, *23*(3), 359–388.
Tardif, R., G. J. Hakim, and C. Snyder (2014), Coupled atmosphere-ocean data assimilation experiments with a low-order climate model, *Clim. Dyn.*, *43*(5-6), 1631–1643.
Tushingham, A., and W. Peltier (1991), Ice-3G: A new global model of late Pleistocene deglaciation based upon geophysical predictions of post-glacial relative sea level change, *J. Geophys. Res.*, *96*(B3), 4497–4523.
van der Wal, W., P. L. Whitehouse, and E. J. Schrama (2015), Effect of GIA models with 3D composite mantle viscosity on GRACE mass balance estimates for Antarctica, *Earth Planet. Sci. Lett.*, *414*, 134–143.
Waelbroeck, C., L. Labeyrie, E. Michel, J. C. Duplessy, J. McManus, K. Lambeck, E. Balbon, and M. Labracherie (2002), Sea-level and deep water temperature changes derived from benthic foraminifera isotopic records, *Quat. Sci. Rev.*, *21*(1), 295–305.
Whitehouse, P. L., M. J. Bentley, G. A. Milne, M. A. King, and I. D. Thomas (2012), A new glacial isostatic adjustment model for Antarctica: Calibrated and tested using observations of relative sea-level change and present-day uplift rates, *Geophys. J. Int.*, *190*(3), 1464–1482.
Winkelmann, R., M. Martin, M. Haseloff, T. Albrecht, E. Bueler, C. Khroulev, and A. Levermann (2011), The Potsdam parallel ice sheet model (PISM-PIK)-Part 1: Model description, *Cryosphere*, *5*(3), 715–726.
Wu, P., and W. Peltier (1984), Pleistocene deglaciation and the Earth's rotation: A new analysis, *Geophys. J. R. Astron. Soc.*, *76*(3), 753–791.